Journal of Colloid and Interface Science 615 (2022) 527–542

Contents lists available at ScienceDirect

Journal of Colloid and Interface Science

journal homepage: www.elsevier.com/locate/jcis

Chemically etched CeO_{2-x} nanorods with abundant surface defects as effective cathode additive for trapping lithium polysulfides in Li-S batteries

Zhen Wei, Ruigang Wang *

Department of Metallurgical and Materials Engineering, The University of Alabama, Tuscaloosa, AL 35487, United States

GRAPHICAL ABSTRACT

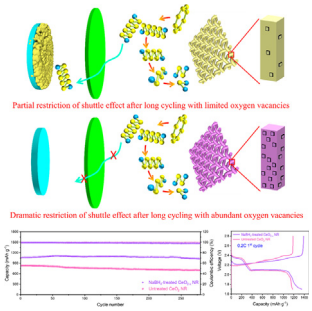

ARTICLE INFO

Article history:
Received 9 December 2021
Revised 16 January 2022
Accepted 25 January 2022
Available online 29 January 2022

Keywords:
Li-S battery
Shuttle effect
Host materials
CeO_2 nanorods
Oxygen vacancies
$NaBH_4$ treatment

ABSTRACT

The commercialization of Li-S batteries has been seriously hindered by the notorious polysulfides shuttling and sluggish redox kinetics. To effectively address these technical issues, in this work, oxygen-deficient CeO_{2-x} nanorods (NR) decorated on free-standing carbon cloth (CeO_{2-x} NR@CC) were used as a promising dual-functional cathode host material to enhance the electrochemical and cycling performance of Li-S batteries. The oxygen-deficient CeO_{2-x} NR were prepared in a facile processing route by tuning the surface structures of pristine CeO_2 NR in strong reducing $NaBH_4$ solution. In contrast to the pristine CeO_2NR@CC control sample, chemically etched CeO_{2-x} NR@CC with abundant implanted oxygen vacancies effectively trapped the polysulfides and dramatically accelerated electron charge transfer, leading to faster redox kinetics. The main working mechanism of CeO_{2-x} NR@CC on the improved electrochemical performance was attributed to chemical binding effect on trapping lithium polysulfides and even promoting the conversion of polysulfides, thanks to reversible Ce^{3+}/Ce^{4+} transformation, oxygen vacancies, and other surface defects. Hence, the CeO_{2-x} NR@CC electrode delivered an outstanding initial capacity of 1358 mAh g^{-1} at 0.2C for the 1st cycle and a superb sulfur utilization of 81%, compared to an initial capacity of 1176 mAh g^{-1} at 0.2C and a sulfur utilization of 70% for the CeO_2 NR@CC electrode. The improved electrochemical performances of the CeO_{2-x} NR@CC electrode can be mainly attributed to the successful adsorption of more dissolvable polysulfides by the dual-functional cathode host materials that combine the physical confinement of conductive CC and the chemical binding of CeO_{2-x} NR with ample surface defects.

* Corresponding author at: 245 7th Avenue, 360 H.M. Comer Hall, United States.
E-mail address: rwang@eng.ua.edu (R. Wang).

https://doi.org/10.1016/j.jcis.2022.01.165
0021-9797/

1. Introduction

Rechargeable secondary batteries have been recognized as a promising technology route to storage and utilize sustainable and environmentally friendly intermittent solar and wind energy, which can compete with and eventually replace traditional fossil fuels. Thanks to the devastating trend of climate change, researchers have been constantly pursuing high energy-efficiency and cost-effective energy storage systems to meet the world's increasing energy demands. In recent years, Li-S batteries or LSBs have been considered as a favorable cost and resource sustainable energy storage system and received enormous attention from scientific community. Part of the reason has to be ascribed to the intrinsic attributes of sulfur cathode such as cost-effectiveness, natural abundance and environmental compatibility [1]. However, the large-scale commercialization of Li–S batteries has been greatly hindered by some formidable technical limitations, particularly the intractable intermediate lithium polysulfide diffusion known as "shuttle effect", leading to low sulfur utilization and fast capacity degradation, and the intrinsically sluggish redox kinetics of sulfur species [2].

To overcome these technical impediments mentioned above for the development of commercially viable Li-S batteries, various sulfur host materials have been innovatively designed aiming to effectively encapsulate sulfur species and mitigate serious shuttling issue of polysulfides. Investigation of carbonaceous materials serving as efficient sulfur host materials have been extensively conducted due to their intrinsic high conductivity, cost-effectiveness and excellent structural tunability (1D, 2D, and 3D structures) [3]. Rapid electronic transport leading to accelerated electrochemical reactions is mainly achieved by the intrinsic superior electrical conductivity of carbonaceous materials [4]. Moreover, effective physical immobilization towards polysulfides migration can be fulfilled by 2D carbonaceous materials like graphene with large surface area and 3D hierarchical porous carbonaceous materials with core–shell structure [5]. However, only limited hinderance of polysulfides diffusion can be achieved by carbonaceous host materials due to poor chemical binding ability towards polysulfides, leading to low sulfur utilization, poor rate capability and fast capacity fading in long term battery life [6]. Therefore, enormous attention has been shifted to various polar host additives, including various metal oxides (such as Ta_2O_5 [7], MnO [8], ZnO [9], Fe_3O_4 [10], V_2O_3 [11]) functioning as efficient adsorbents that can chemically bind polysulfides. However, the intrinsic poor electrical conductivity of metal oxides leading to sluggish redox kinetics needs to be further enhanced for the development of commercially viable Li-S batteries.

Metal oxides and metal sulfides used as sulfur host materials have been receiving increasing attention from scientific community [12–17]. For instance, Dong et al. [12] reported that bronze TiO_2 (TiO_2-B) nanosheets can chemically bond with carbon as a promising host material for rechargeable Li-S batteries. As a result, the TiO_2-B/S electrode demonstrated high discharge capacity (1165 mAh g^{-1} at 0.2C) and superb rate capability (244 mAh g^{-1} at 5C). Chen et al. [13] reported that MnO_2 nanosheets were *in-situ* grown on hollow nitrogen-doped micropore-rich carbon (NMRC) to form NMRC/S@MnO_2 nanocomposite, which led to high areal sulfur loading for the improved the Li-S batteries' electrochemical performances. As a result, the NMRC/S@MnO_2 nanocomposite can achieve a high sulfur loading of 72% and demonstrate an excellent initial discharge capacity of 1144 mAh·g^{-1}, while maintaining a reversible discharge capacity of 1023 mAh·g^{-1} after 200 cycles at 0.2C. The excellent electrochemical performance was attributed to the synergistic dual encapsulation (structural confinement and chemisorption). In addition, Meng et al. [16] reported that $MoSe_2$ nanosheets were anchored on hollow carbon spheres with mesoporous walls through a simple solvothermal method. The boosted electrical transfer of $MoSe_2$ nanosheets was fulfilled by the formation of interfacial C-Se bonds. High chemical affinity to lithium polysulfides and propelled conversion kinetics were achieved by ultrathin $MoSe_2$ nanosheets with abundant edge defects. Consequently, the $MoSe_2$@MCHS-S electrode displayed excellent discharge capacity and superb cycling stability.

Defect engineering has also played an increasingly critical role in the development of Li-S battery [18–21]. Tian et al. [18] reported that the inhibition of polysulfide shuttling and enhancement of battery performance can be fulfilled by an anion-deficient design of antimony selenide (Sb_2Se_{3-x}). The sulfur electrochemistry was significantly promoted and stabilized by the multifunctional LiPS (lithium polysulfides) barrier, rendering superior Li–S battery performance. The battery assembled with Sb_2Se_{3-x} demonstrated superb cyclability over 500 cycles at 1.0C with a minimum capacity decay rate of 0.027% per cycle. Wang et al. [19] developed an oxygen-deficient niobium oxide (Nb_2O_{5-x}) framework with 3D ordered macroporous architecture and carbon nanotubes (CNTs) embedding, functioning as an excellent sulfur trapper and catalytic promoter for polysulfide conversion. It is important to mention that CNTs were designed as "antennae" embedded within the Nb_2O_{5-x} framework. This innovative design not only provides a highly conductive framework but also increases the oxygen deficiency. Consequently, the S-Nb_2O_{5-x}/CNTs electrode achieved a superior rate capability with 741 mAh g^{-1} at 5C. Meanwhile, Yang et al. [21] reported that introducing either donor defects (P dopants) or acceptor defects (Ni vacancies) through P-doping or $NaBH_4$-etching is a promising method to modulate the electronic and valence states of metal active sites in hollow carbon-encapsulated $Ni_3ZnC_{0.7}$ (denoted as C/$Ni_3ZnC_{0.7}$) nanospheres. The remarkable decrease in the electron density of Zn active sites in C/$Ni_3ZnC_{0.7}$-P5 is fulfilled by P dopants and accompanied Zn vacancies. In addition, a dramatic increase of the Ni^{2+} species in C/$Ni_3ZnC_{0.7}$-B1 nanospheres was achieved by the Ni vacancies. In contrast to C/$Ni_3ZnC_{0.7}$ and C/$Ni_3ZnC_{0.7}$-P5, C/$Ni_3ZnC_{0.7}$-B1 with more Ni^{2+} species displayed better adsorption capability and catalytic ability to facilitate the conversion of polysulfides, leading to superior rate performance up to 4.0C (525.6 mA h g^{-1}).

The majority of the shuttling alleviation approaches reported to date has been concentrated on the development of novel sulfur host materials, interlayers or separator modifiers. Although enormous progress has been made, these reported approaches are still incapable of achieving the full electrochemical potential of Li-S batteries and some are also expensive to carry out. Interestingly, several recently published reports have demonstrated that the implanting oxygen-deficient structure could strengthen the polysulfides adsorption capability of sulfur host materials and improve the electronic conductivity of metal oxides. For instance, Lv et al. [22] reported that oxygen-deficient ferric oxide (Fe_2O_{3-x}) nanoparticles synthesized by a simple lithiothermic reduction approach were used as a cost-effective electrochemically catalytic sulfur host material. The concentration of oxygen deficiencies in Fe_2O_{3-x} could be effectively implanted and tuned by changing the amount of lithium. The electrochemical performances of Li-S batteries assembled with Fe_2O_3 and highly catalytic Fe_2O_{3-x} were compared and analyzed. Experimental results exhibited that Fe_2O_{3-x} had a strong polysulfides adsorption capability and was able to facilitate the electrochemical conversion to insoluble Li_2S. In addition, Li et al. [23] reported that a sea urchin-structured multifunctional sulfur host material was developed for high-performance Li-S batteries by anchoring ultrafine Co nano-dots onto oxygen-deficient TiO_2 (Co@TiO_{2-x}). The formation of oxygen vacancies in the TiO_2 substrate was achieved by the introduction of ultrafine Co nano-dots

leading to the successful lattice doping and reduction of TiO_2. Homogeneous sulfur distribution, tunable electronic conductivity and accelerated polysulfides conversion reaction were fulfilled by the synergistic effect of defect engineering and nano-dot incorporation. In another report, Wang et al. [24] described that porous double-shelled oxygen-deficient Co_3O_{4-x} microspheres with strong polysulfides affinity were developed to effectively address shuttling issue for high-performance Li-S batteries. The formation of abundant oxygen deficiency on original Co_3O_4 microspheres was fulfilled by proper reduction treatment in hydrogen, resulting in accelerated charge transfer and mitigated polarization issue. As a result, the $S@Co_3O_{4-x}$ composite cathode demonstrated superior cycling performance and rate capability.

The aforementioned methods to generate oxygen vacancies such as proper reduction treatment seem quite thermally and processably cumbersome. Compared with other complicated approaches, in the current study, we applied a facile chemical etching treatment with a strong reducing sodium borohydride ($NaBH_4$) solution to obtain oxygen deficient CeO_2. Based on our recently reported work [25], CeO_2 nanorods can successfully trap polysulfides by the termination planes (110)/(100)/(111) with strong adsorption capability and various surface defects. In order to further fulfill the electrochemical potential of CeO_2 nanorods and meanwhile take the fabrication cost of the sulfur host materials into account, herein, we demonstrated a chemically modified CeO_2 nanorods through a simple $NaBH_4$ solution treatment to provide more polysulfides anchoring sites and maximize the chemical adsorption capability of CeO_2 nanorods. A correlation study between the alteration of the surface structure of CeO_2 host and the electrochemical performance was provided. This work exhibits the promise of defect engineering for the enhanced adsorption capability and improved catalytic conversion leading to the further development of high-performance Li–S batteries.

2. Experimental section

2.1. Synthesis of pristine CeO_2 nanorods

CeO_2 nanorods in this work were prepared by using a facile hydrothermal method as reported previously [26–29]. First of all, 88 mL of 0.1 M $Ce(NO_3)_3{\cdot}6H_2O$ (Acros Organics, 99.5%) and 8 mL of 6.0 M NaOH (VWR, 99%) solutions were mixed and subsequently the mixed solution was stirred vigorously for ~ 15 s. Secondly, the mixed solution was transferred into a Teflon liner with 200 mL capacity and subsequently the Teflon liner was placed into a stainless-steel autoclave. Thirdly, the autoclave was heated and kept at 90 °C for 48 h. Finally, the sample was filtered and subsequently was rinsed with DI water and ethanol, which was followed by drying at 60 °C for 12 h to get pristine CeO_2 nanorods (CeO_2 NR) powder.

2.2. Preparation of oxygen-deficient CeO_{2-x} by $NaBH_4$ chemical etching

The obtained CeO_2 NR powder underwent a chemical etching treatment using $NaBH_4$ solution as described in the following steps. Firstly, CeO_2 NR powder was dispersed into DI water in a 250 mL beaker and 6 wt% of $NaBH_4$ powder (weight percent = $NaBH_4/(NaBH_4 + CeO_2) \times 100\%$) was dispersed into the CeO_2 /water suspension, which was followed by vigorously stirring for 12 h on a magnetic stirrer. Secondly, the sample was filtered and dried at 60 °C for 12 h to obtain oxygen-deficient CeO_{2-x}.

2.3. Preparation of CeO_2 NR@CC and CeO_{2-x} NR@CC

Commercial free-standing carbon cloth (Fuel cell earth, 20 cm × 20 cm, thickness = 0.381 mm, density = 1.75 g/cm^3) was punched out into circular disks with 15 mm diameter. The previously obtained chemically etched CeO_{2-x} NR powder and untreated CeO_2 NR powder were separately dispersed into *N*-methyl-2-pyrrolidone (NMP) solvent. The homogeneous CeO_{2-x} NR and CeO_2 NR suspensions were separately dropped onto the circular discs of carbon cloth. The circular disks were subsequently transferred into the vacuum drying oven and underwent the vacuum drying at 60 °C for 12 h. After drying, the obtained circular discs were referred to as CeO_{2-x} NR@CC and CeO_2 NR@CC thereafter. The mass loading of CeO_{2-x} NR and CeO_2 NR was 1 mg for each electrode.

The circular disks of CeO_2 NR@CC and CeO_{2-x} NR@CC were coated with a slurry prepared by mechanically mixing super P carbon black (Alfa Aesar, ≥ 99%) used as conductive agent and polyvinylidene fluoride (PVDF) used as binder in *N*-methyl-2-pyrrolidone (NMP) solvent, which were followed by vacuum drying at 60 °C overnight. These two CeO_2 coated CC disks were used as the cathodes in this work. In this research, as 3D inter-connected CC can physically confine the polysulfides migration and CeO_{2-x} NR with copious implanted oxygen vacancies and other surface defects can chemically adsorb more polysulfides, CeO_{2-x} NR@CC is called dual-functional cathode host material.

In this work, two methods were used to load CeO_{2-x} NR onto CC: 1) drop diluted CeO_{2-x} NR slurry on CC layer by layer on both sides of CC; 2) immerse CC into the CeO_{2-x} NR slurry for a fixed time. It was found that the first method was more convenient to quantitively measure the amount of CeO_{2-x} NR in CeO_2 NR@CC by measuring the mass change of CC before and after loading. As evidenced in the SEM images, a uniform and well-dispersed distribution of CeO_{2-x} NR onto the carbon cloth can be fulfilled. After CeO_{2-x} NR loading, other additives (the carbon black, PVDF, conductive agent, and binder) were added in the subsequent steps. SEM and EDX analysis were carried out to characterize the distribution and uniformity of CeO_{2-x} NR on CC.

2.4. Preparation of Li_2S_6 solution and polysulfide adsorption test

The blank liquid electrolyte was prepared by mixing 1.0 M lithium bis(trifluoromethane) sulfonimide (LiTFSI) (Adipogen Corp Ms, ≥ 99%) with 0.5 M $LiNO_3$ (Alfa Aesar, 99.999%) in dioxolane: dimethoxyethane (DOL:DME) (1:1 by volume ratio) (Alfa Aesar, 99%). 1.0 M Li_2S_6 solution was prepared by directly adding sublimed S powder (Alfa Aesar, ≥ 99.5%) and Li_2S powder (Alfa Aesar, ≥ 99.9%) with a molar ratio of 5:1 into the blank liquid electrolyte. To thoroughly dissolve sulfur and Li_2S, the previously obtained solution was heated on a hot plate at 60 °C and was kept vigorously stirring for 24 h inside an Argon-filled glovebox. Finally, the solution had a reddish color without obvious sediment. To carry out polysulfide adsorption test, 1.0 M polysulfide solution was diluted to 6.0 mM Li_2S_6 solution. 25 mg of untreated CeO_2 NR and $NaBH_4$-treated CeO_{2-x} NR powders were put separately into two different vials with 2 mL of 6.0 mM Li_2S_6 solution. Photos were taken at the beginning of the test and after 10, 20, 60, and 180 mins of the adsorption.

2.5. Cell assembly

The whole cell assembly procedure was carried out in an Ar-filled glovebox (the O_2 and H_2O contents were lower than 0.1 ppm). The 2032-type coin cells assembly was conducted by using pure lithium foil as the anode and Celgard 2400 membrane as the separator, respectively. Firstly, 10 μL of Li_2S_6 catholyte solution was added drop by drop onto the discs of CeO_2 NR@CC and CeO_{2-x} NR@CC, achieving an areal sulfur loading of 1 mg cm^{-2}. Secondly, 30 μL of the blank electrolyte (1.0 M LiTFSI and 0.5 M $LiNO_3$ dissolved in mixed DME and DOL solvent with a volume ratio of

1:1) was dropped onto each of the cathode discs. Thirdly, the separator was put on the top of the cathode discs, which was followed by adding drop by drop another 30 μL of the blank electrolyte. Subsequently, the lithium metal anode was placed on the top of the separators. Then, the spacer made of stainless steel was placed on the top of the Li metal anode. Following, the spring made of stainless steel was placed on the top of the spacer. Finally, the coin cells were subjected to crimping. After being crimped by a crimper, the assembled coin cells went through a resting procedure for 12 h.

2.6. Materials characterization

The Raman spectroscopy was performed by using a Horiba LabRAM HR 800 Raman spectrometer equipped with wide spectral window (100 ~ 1200 cm^{-1}) and a 100 long-working-distance objective (NA = 0.60). A silicon single-crystal wafer (520.7 cm^{-1}) was used to implement the calibration of Raman spectrometer. The surface chemistry of the powders was analyzed by X-ray photoelectron spectroscopy (XPS) using a Kratos Axis Ultra DLD spectrometer equipped with monochromatic Al Kα radiation ($h\nu$ = 1486.6 eV) under ultra-high vacuum (10^{-10} Torr). Resulting from possible charging issue, the calibration of the binding energy drift was conducted by using the carbon C 1 s peak (284.8 eV). The fitting and deconvolution of the spectrum peaks were carried out by using CasaXPS software. The morphologies of the investigated CeO_2 NR@CC and CeO_{2-x} NR@CC powders were characterized by scanning electron microscopy (SEM, JEOL 7000 FE) coupled with an Oxford Instruments energy dispersive X-ray spectrometer (EDS).

2.7. Electrochemical measurement

The galvanostatic charge discharge cycling was measured on an MTI battery tester with a voltage window (1.7 V ~ 2.8 V) and various C-rates (1C = 1675 mAh g^{-1}). A Gamry Potentiostat/Galvanostat workstation (Gamry Interface 1000E) was used to not only perform the cyclic voltammetry (CV) measurement with a voltage window (1.7 ~ 2.8 V) at a scan rate of 0.1 mV s^{-1}, but also carry out the electrochemical impedance spectroscopy (EIS) measurement with the frequency range of 0.01–10^5 Hz. The testing temperature for all the electrochemical measurements was 25 ℃.

3. Results and discussion

3.1. Morphological characterization before cycling

Fig. 1 schematically illustrates the preparation processes of the untreated CeO_2 NR powder and chemically etched CeO_{2-x} NR powder using $NaBH_4$ and the detailed procedures are provided in the experimental section. **Fig. S1** displays the XRD patterns of untreated CeO_2 nanorods powder and $NaBH_4$-treated CeO_{2-x} nanorods powder. The representative diffraction peaks can be seen at 28.5, 33.1, 47.5, 56.3, 59.1, 69.4, 76.7, 79.1 and 88.4° for untreated CeO_2 nanorods and $NaBH_4$-treated CeO_{2-x} nanorods, corresponding to face-centered cubic CeO_2 phase with fluorite structure (JCPDS: No.34–0394).

As shown in Fig. 2, the morphologies of the CeO_2@CC and CeO_{2-x}@CC hosts were examined using SEM. As presented in the SEM images taken at different magnifications (Fig. 2a–c and Fig. 2e–**g**), the free-standing carbon cloth functioning as the host material substrate is composed of 3D interconnected carbon fibers with strong mechanical strength. It can be easily observed that pristine CeO_2 NR particles and $NaBH_4$-treated CeO_{2-x} NR particles tightly adhere to the carbon fibers and are embedded throughout the whole carbon cloth framework. The successful fabrication of CeO_2@CC and CeO_{2-x}@CC and distribution of CeO_2/CeO_{2-x} on CC were further validated by EDS elemental mapping (Fig. 2d and 2h), which show the presence of uniformly dispersed Ce, O, S elements.

To further identify the defects due to the chemical etching of strong reducing $NaBH_4$ on the surface of CeO_2, TEM was carried out and HRTEM images provided convincing evidence as shown in **Fig. S2a–b**. It is worth noting that the lattice fringes discontinuities or micropores can be easily observed after chemical etching (**Fig. S2b**), corresponding to the "implanted" surface defects on CeO_2 [30–32]. Meanwhile, the enlarged HRTEM images of the untreated CeO_2 sample (**Fig. S2a**) show more uniform lattice structure.

In addition, as shown in the EDS spectrum of **Fig. S3**, except for Ce, O, and C, no observable or significant amount of B and Na for the $NaBH_4$-treated CeO_{2-x} powder sample was detected after the rinsing process before using it in the battery cell. This indicates that B or Na doping in CeO_{2-x} lattice can be neglected.

3.2. Raman spectroscopy

To further gain insights of coordination environment and defects (i.e., oxygen vacancies, Ce^{3+}/Ce^{4+}, and lattice distortion), Raman spectroscopy was carried out on the pristine CeO_2 powder and chemically etched CeO_{2-x} powder. Apart from the obvious characteristic F_{2g} peak (Fig. 3a), one easily observable band at around 255 cm^{-1} is correlated with doubly degenerate TO mode (2TA) of CeO_2 and another easily perceptible band situated near 600 cm^{-1} corresponds to the defect-induced band (D band), which can be used for estimating the concentration of the oxygen vacancy defects [33]. In addition, as shown in Fig. 3b-d, the noticeable shift of three representative peaks (4.99 cm^{-1} shift for 2TA band, 4.45 cm^{-1} shift for D band and 1.05 cm^{-1} shift for F_{2g} peak) confirms the impact of embedding oxygen vacancies into pristine CeO_2 lattice [34].

3.3. Electrochemical characterization

To understand the effect of oxygen-deficiency in CeO_{2-x} on the redox conversion of polysulfides, CV measurements of the CeO_2@-CC and CeO_{2-x}@CC cells were implemented. During the cathodic scan for the 1st cycle of CV measurements (Fig. 4a), both the CeO_2@CC and CeO_{2-x}@CC cells exhibit two related reduction peaks at around 2.3 and 2.0 V, which are assigned to the electrochemical reduction of sulfur into soluble polysulfides ($S_8 \rightarrow Li_2S_x$, $x \geq 4$, referred to as C I) and the subsequent reduction of long-chain polysulfides into insoluble Li_2S_2/Li_2S ($Li_2S_x \rightarrow Li_2S_2/Li_2S$, $x \geq 4$, referred to as C II), respectively [35]. In the following anodic scan, two adjacent characteristic oxidation peaks correspond to the reverse conversion from insoluble Li_2S_2/Li_2S to the long-chain polysulfides ($Li_2S_2/Li_2S \rightarrow Li_2S_x$, $x \geq 4$, referred to as A II) and final oxidation into element sulfur ($Li_2S_x \rightarrow S_8$, $x \geq 4$, referred to as A I) [36]. It is well acknowledged that the conversion between soluble polysulfides to insoluble Li_2S_2/Li_2S can deliver the larger segment of the specific capacity of Li-S battery. Thus, the cathodic peak (C II) and the corresponding oxidation peak (A II) play a more pivotal role in delivering high specific capacity of Li-S battery. It is worth noting that the CeO_{2-x}@CC cell demonstrates a higher redox current compared with the counterpart CeO_2@CC cell. Specifically, the current response of the A II peak and the C II peak of the CeO_{2-x}@CC cell (4.31 mA and 4.72 mA) is 12.8% and 21.6% higher than those of the CeO_2@CC cell (3.82 mA and 3.88 mA), respectively, implying improved redox kinetics of polysulfide transformation due to the superior catalytic activity of oxygen-deficient CeO_{2-x} [37]. Moreover, the CeO_{2-x}@CC cell displays the minimal peak separation of A II peak and C II peak compared with the counterpart CeO_2@CC

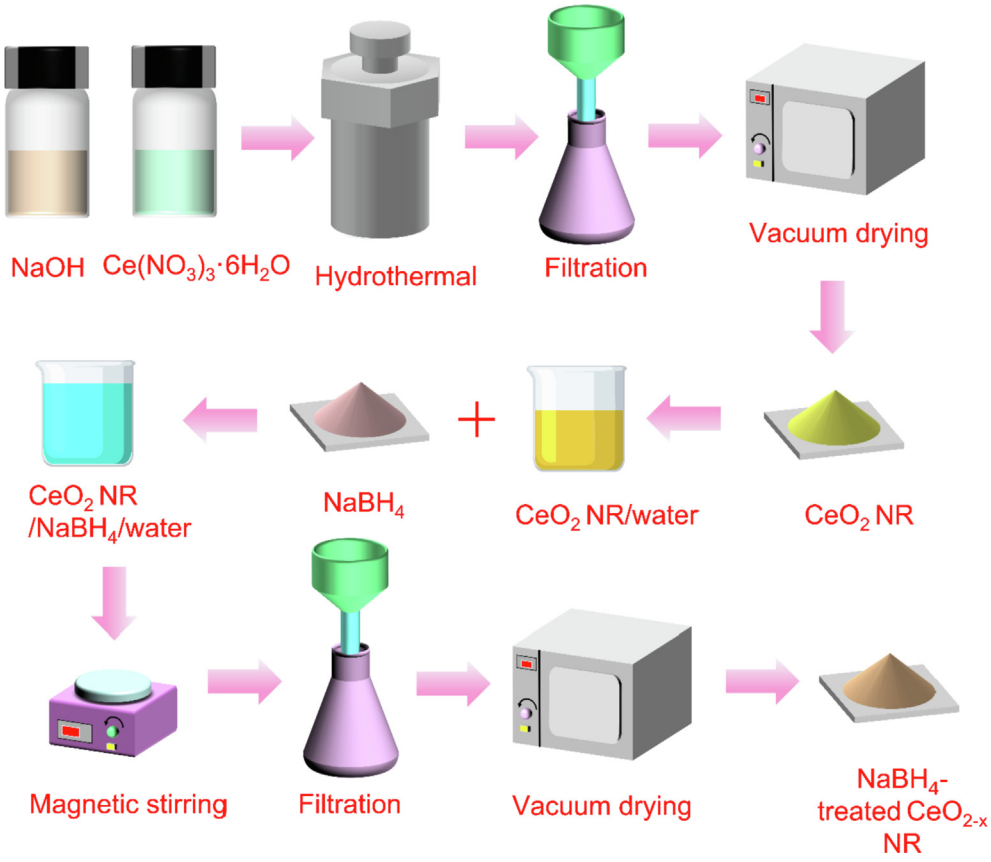

Fig. 1. Schematic illustration of the fabrication processes of CeO_2 NR powder and $NaBH_4$-treated CeO_{2-x} NR powder.

cell. To be specific, the potential difference of the CeO_{2-x}@CC cell (346 mV) is smaller than that of the CeO_2@CC cell (354 mV), demonstrating the better sulfur utilization and smaller polarization inside the cell, which can be attributed to the better sulfur distribution fulfilled by the increase of electrochemically active defective sites (oxygen vacancies, Ce^{3+}/Ce^{4+}, and lattice distortion) [38]. Fig. 4b displays the 3rd cycle of CV measurements for both samples and Fig. 4c-d compare the CV profiles for the initial three cycles for the cells with the chemically etched CeO_{2-x} and untreated CeO_2. Apart from the larger redox current of A II and C II peaks (Fig. 4b), the potential difference of oxygen-deficient CeO_{2-x} for the 3rd cycle (319 mV) is much smaller than that of pristine CeO_2 (362 mV), indicating higher electrical conductivity and better reversibility during the galvanostatic cycling [39]. The chemically etched CeO_{2-x} (Fig. 4c) exhibits a small negative shift in the anodic peak (A II peak), demonstrating a decrease in cell polarization and improved kinetics of polysulfide redox [39]. However, for the untreated CeO_2 (Fig. 4d), the anodic peak (A II peak) shows a subtle positive shift, indicating an increase in cell polarization and sluggish redox kinetics due to the lack of promotion on polysulfides conversion [10].

The catalytic performance of $NaBH_4$-treated CeO_{2-x} NR was further explored through symmetrical batteries at the scan rate of 1 mV s^{-1}. As shown in **Fig. S4**, it was observed that $NaBH_4$-treated CeO_{2-x} NR has two pairs of sharp redox peaks and the current response was obviously higher, which demonstrates that $NaBH_4$-treated CeO_{2-x} NR can promote the electrochemical redox reaction of polysulfides.

Galvanostatic discharge–charge was carried out to measure the capacity and cycling reversibility of the assembled coin cells with the CeO_2 NR@CC and CeO_{2-x} NR@CC electrodes and further to assess the effectiveness of oxygen-deficient CeO_{2-x} NR@CC on the electrochemical performance of Li-S batteries. As shown in Fig. 5a, the discharge curves of the CeO_2 NR@CC and CeO_{2-x} NR@CC cells at 0.2C demonstrate two voltage plateaus, which is consistent with the CV results. The CeO_{2-x} NR@CC electrode delivers an excellent discharge capacity of 1358 mAh g^{-1} at 0.2C for the first galvanostatic cycle, demonstrating a superior sulfur utilization of 81%. In contrast, the CeO_2 NR@CC cell displays an "unsatisfactory" discharge capacity of 1176 mAh g^{-1}, exhibiting a sulfur utilization of 70%. As shown in Fig. 5b-c, the CeO_{2-x} NR@CC cell demonstrates an outstanding discharge capacity of 1287 mAh g^{-1} for the 100th cycle. In addition, the capacity retention is as high as 94.8% and the exhibited capacity fading rate is only 0.052% per cycle in a long 100 galvanostatic cycles. However, for the 100th cycle of the CeO_2 NR@CC electrode, the preserved discharge capacity is 1077 mAh g^{-1} after 100 cycles. This result implies a slightly higher capacity decay after 100 cycles at 0.2C with a smaller capacity retention of 91.6%. Better results seen from the CeO_{2-x} NR@CC cell can be ascribed to the accelerated polysulfide redox and the alleviated electrode polarization by embedding adequate oxygen vacancies [40]. Furthermore, the delivered capacity of the CeO_{2-x} NR@CC cell is superior compared with that of the CeO_2 NR@CC cell at different rates (Fig. 5d). Upon continuous cycling with increasing current densities, the CeO_{2-x} NR@CC cell only exhibits a marginal drop in the capacities at high rates and the capacities are immediately recovered with their reversal, implying the rapid polysulfide transformation rates, resulted from a successful inhibition of polysulfides diffusion and efficient acceleration of redox kinetics [41]. In contrast, the CeO_2 NR@CC cell shows an inferior capacity at each

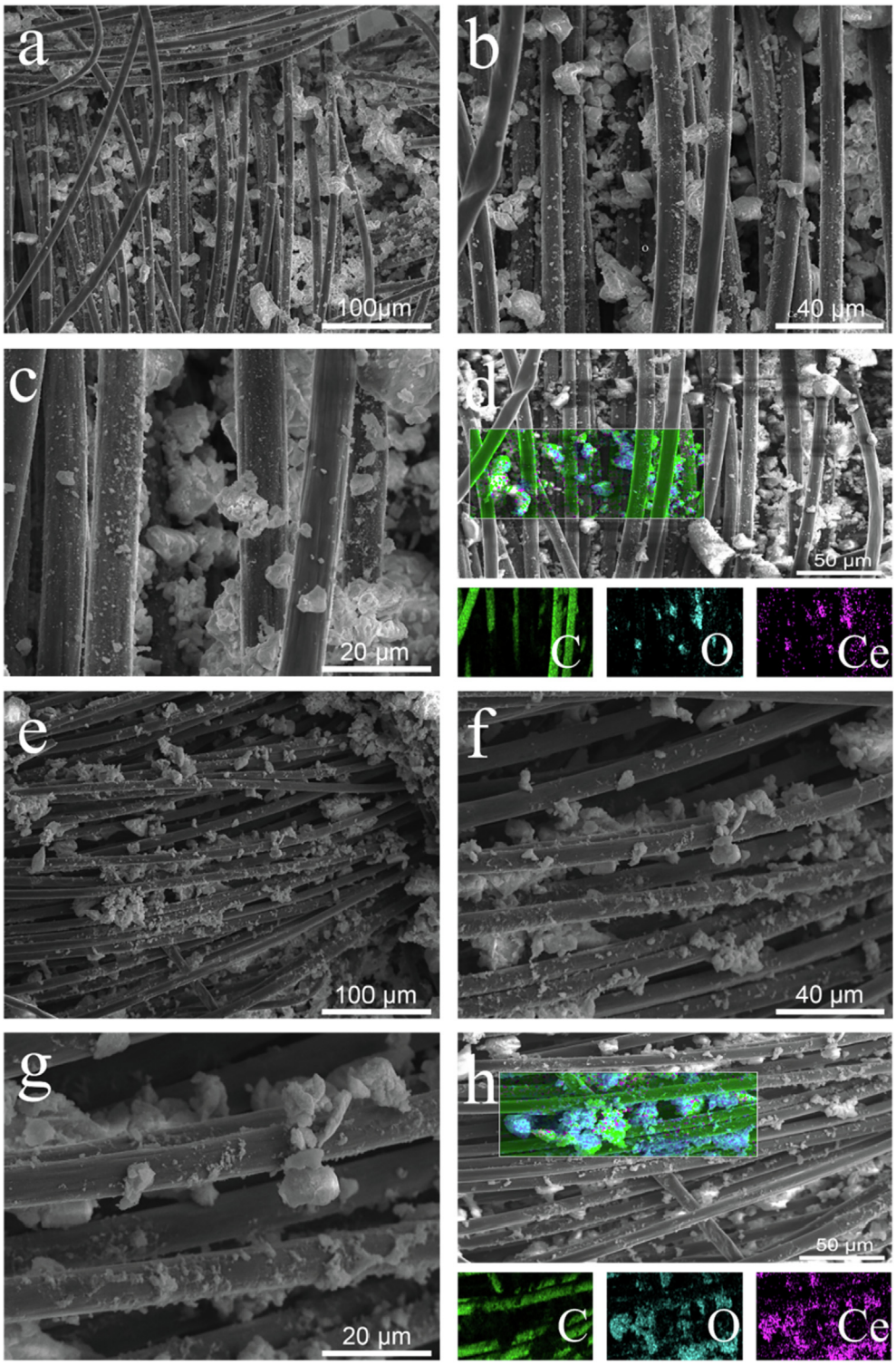

Fig. 2. SEM images of (a–c) CeO_2@CC and (e-f) CeO_{2-x}@CC taken at different magnifications; EDS elemental mapping of (d) CeO_2@CC and (h) CeO_{2-x}@CC.

rate. The CeO_{2-x} NR@CC cell exhibits much better electrochemical performance than the CeO_2 NR@CC cell at high current densities (Fig. 5e–f). The CeO_{2-x} NR@CC cell (Fig. 5e) demonstrates excellent cycling stability as well as higher initial capacity compared with the CeO_2 NR@CC cell. After 280 galvanostatic cycles at 1C, the capacity retention of the CeO_{2-x} NR@CC cell (96.8%) is much higher than that of the CeO_2 NR@CC cell (84.0%). Hence, structural tunability of the CeO_2 cathode additive by the introduction of ample oxygen deficiencies can clearly enhances the electrochemical performance of Li-S batteries [42]. The CeO_2 NR@CC cell (Fig. 5f) delivers an initial capacity of 759 mAh g^{-1} and reversible capacity of 650 mAh g^{-1} after 350 cycles at 2C, corresponding to a mediocre capacity retention of 85.6%. In comparison, for the CeO_{2-x} NR@CC electrode cycled at 2C, a high initial capacity of 943 mAh g^{-1} and

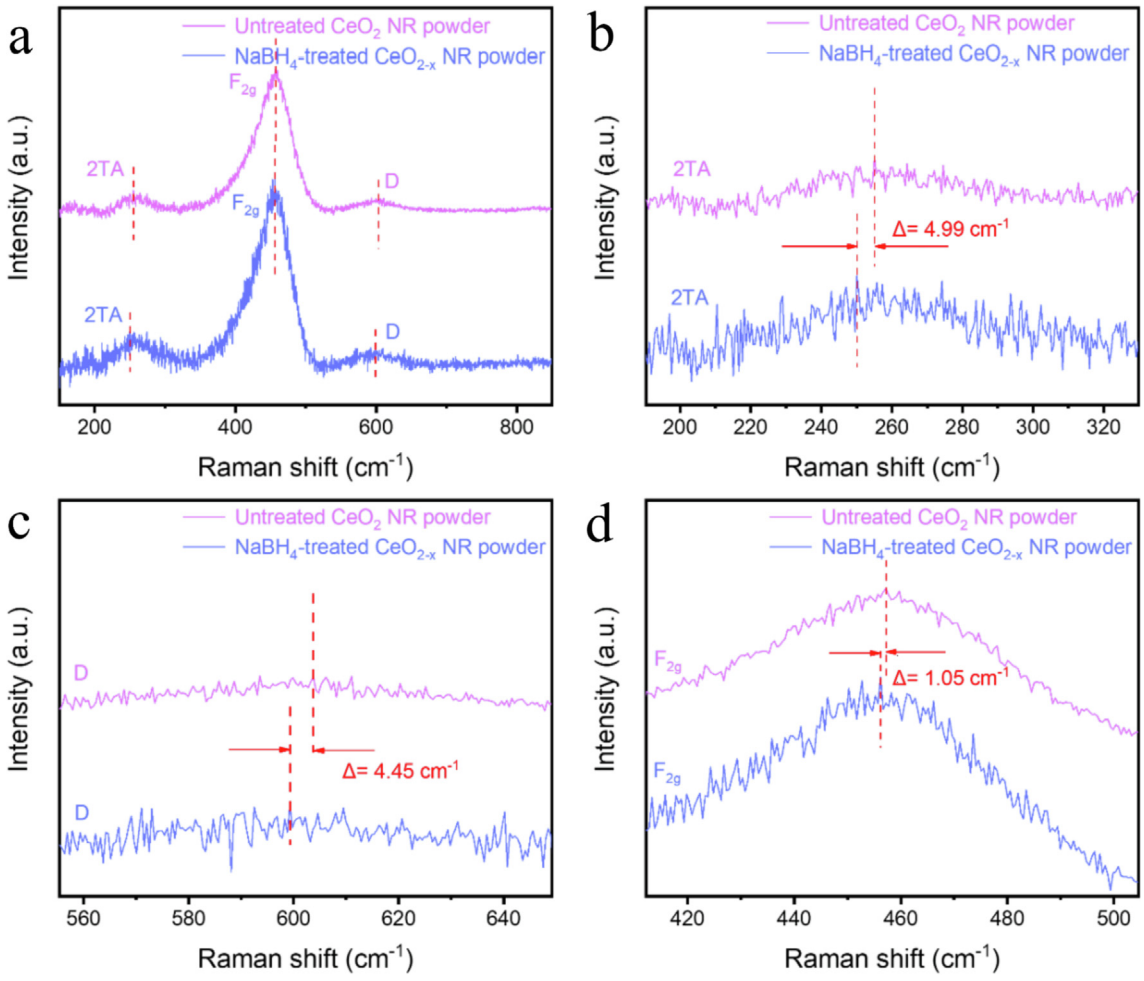

Fig. 3. Raman spectrum comparison of (a–d) CeO_2 and CeO_{2-x} powders.

excellent reversible capacity of 863 mAh g^{-1} after 350 galvanostatic cycles are demonstrated, along with quite stable voltage plateau over the whole cycling process. The capacity retention is as high as 91.5% and the shown capacity decay rate is only 0.024% per cycle in a prolonged 350 cycles. We hypothesize that the number disparity in electrochemically active sites for anchoring polysulfides led to this performance difference at the high current density [43].

The electrochemical performance comparison between the chemically etched CeO_{2-x} NR and the pristine CeO_2 NR with a higher areal sulfur loading (3 mg cm^{-2}) and a smaller amount of electrolyte (40 μL) is displayed in **Fig. S5**. The cycling performance of the chemically etched oxygen-deficient CeO_{2-x} NR electrode is clearly better than that of the pristine CeO_2 NR electrode with higher areal sulfur loading when cycling at the current density of 0.2C. **Fig. S5a–d** exhibit the chemically etched CeO_{2-x} NR electrode delivers specific discharge capacity of 1098, 1046, and 1015 mAh g^{-1} at the 1st , 50th and 100th cycles, respectively, which are higher than those of the untreated CeO_2 NR cathode (939 mAh g^{-1} at the 1st cycle, 881 mAh g^{-1} at the 50th cycle and 886 mAh g^{-1} at the 100th cycle).

In addition, a battery cell with 6 mg cm^{-2} areal sulfur loading and 30 μL electrolyte was also assembled and tested. The chemically etched CeO_{2-x} NR electrode still displayed better electrochemical performance than the pristine CeO_2 NR electrode (**Fig. S6**). A performance comparison is given in **Table S1** including some previously reported Li-S batteries containing CeO_2.

3.4. Microstructure analysis of the disassembled cells

To understand chemical polysulfides adsorption capability, morphological characterization of Li anode surfaces from the disassembled CeO_{2-x}NR@CC and CeO_2NR@CC cells after 350 galvanostatic cycles at 2C was carried out by SEM to gain information about the structural and chemical changes. The anode with CeO_2-NR@CC (Fig. 6a–c) exhibits a rough morphology with congregated dendrites and is full of polysulfide deposition [44]. It can be seen in Fig. 6a–c that Li metal anode with the CeO_2NR@CC electrode after cycling is loosely packed and has numerous cracks formed on the surface, implying severe surface corrosion of Li anode induced by shuttle effect [45]. However, the surface of Li anode with CeO_{2-x}NR@CC seems relatively smooth and the formed dendrites are small and hardly visible (Fig. 6h–**j**) [46], suggesting that the addition of CeO_{2-x}NR apparently alleviates the dissolution and diffusion of polysulfides in the organic electrolyte. Therefore, the side reaction between Li metal anode and polysulfides leading to serious surface corrosion is successfully mitigated. Moreover, the EDS elemental mapping of Li anode with CeO_{2-x}NR@CC shows a much less deposition of sulfur element than the one with CeO_2-NR@CC (Fig. 6d–**g and 6k–n**). These results substantiate that enormous oxygen vacancies induced by a simple $NaBH_4$ solution treatment are able to successfully restrict the polysulfide shuttling and mitigate the Li dendrite growth.

Fig. 7a–b show the SEM cross-sectional images of the cycled Li anodes after 350 cycles at 2C. After cycling, the thickness of the

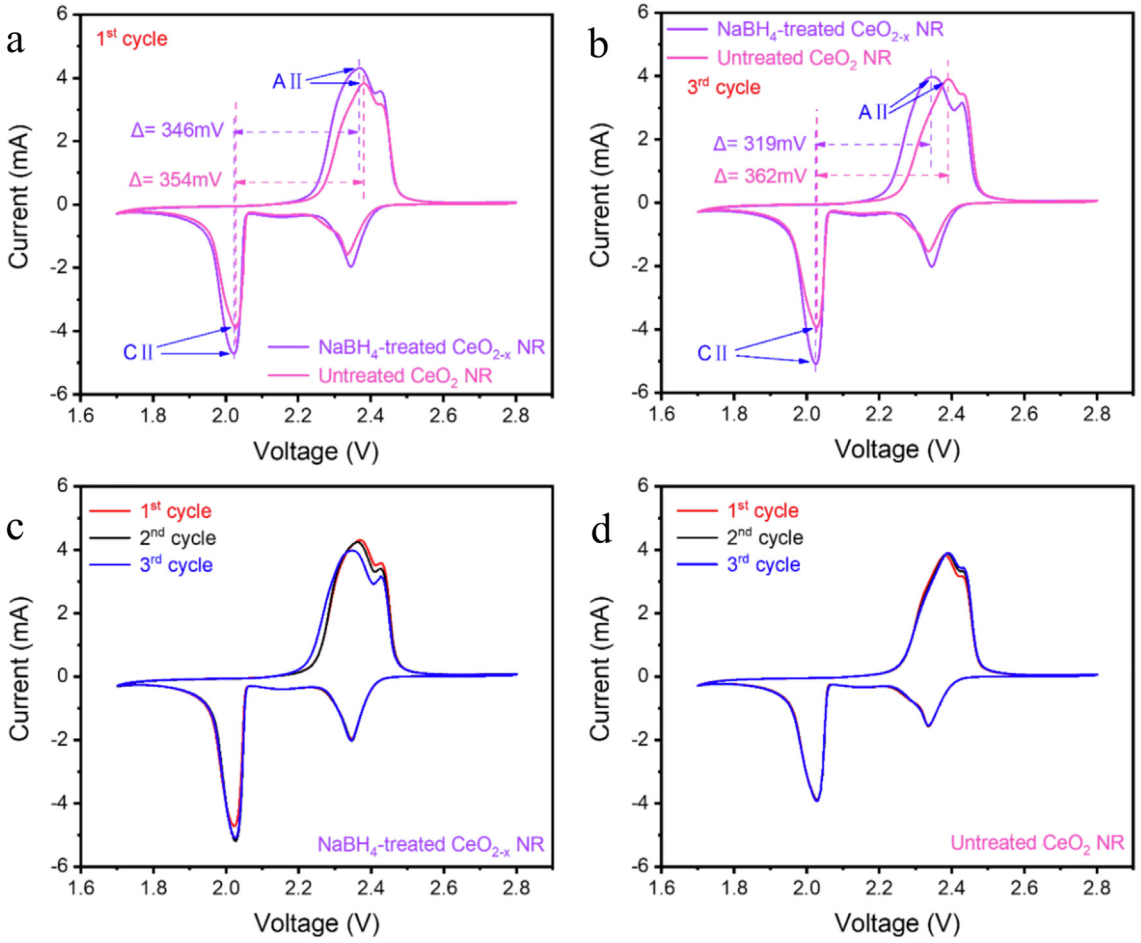

Fig. 4. CV comparison of the assembled cells with (a–b) untreated CeO_2 and $NaBH_4$-treated CeO_{2-x} additives for the 1st and 3rd cycles and the CV curves during the first three cycles (c–d) for $NaBH_4$-treated CeO_{2-x} and untreated CeO_2 additives.

corrosion layer on the cycled Li anode with the CeO_{2-x}NR@CC electrode is thinner compared to that of the Li anode with the CeO_2-NR@CC electrode. To measure the thickness and elemental diffusion of the corrosion layer, EDS line scans for S element were implemented. It is worth mentioning that S element was detected on the corrosion layer, providing powerful evidence of the severely corroded Li metal anode caused by serious shuttle effect [47]. Fig. 7c-d exhibit the EDS line scan results on the cross-sections of the cycled Li anode with the CeO_{2-x}NR@CC electrode and CeO_2-NR@CC electrode. As displayed in Fig. 7d, the sulfur signal can be detected deep into the majority of cycled Li metal anode (~500 μm). In contrast, for the CeO_{2-x}NR@CC electrode, the sulfur signal is concentrated in a layer (~150 μm) between Li anode surface and slightly below the surface (Fig. 7c).

3.5. Adsorption test

In order to validate the adsorption capability for polysulfides, a simulation chemisorption experiment was carried out by dispersing host materials (untreated CeO_2 powder and $NaBH_4$-treated CeO_{2-x} powder) into polysulfides solutions (Li_2S_6 in DOL/DME) [48]. The polysulfides adsorption capability of two different host materials (untreated CeO_2 powder and $NaBH_4$-treated CeO_{2-x} powder) was exhibited by the color change of the solutions recorded using digital photographs. When the untreated CeO_2 powder and $NaBH_4$-treated CeO_{2-x} powder were added to the Li_2S_6 solution at the time = 0 min (Fig. 8a), there was no apparent difference, and the solution was dark yellow. As shown in Fig. 8b–d, the Li_2S_6 solution containing the $NaBH_4$-treated CeO_{2-x} powder changed from dark yellow to light yellow at a rapid pace (at the time intervals = 10, 20, 60 mins). In comparison, the Li_2S_6 solution containing the untreated CeO_2 powder demonstrated a slower decolorization. After 180 mins (Fig. 8d), the color of the Li_2S_6 solution containing the $NaBH_4$-treated CeO_{2-x} powder was much lighter and more transparent than that of the control sample [49]. After 180 mins, Li_2S_6 solution with the untreated CeO_2 powder and $NaBH_4$-treated CeO_{2-x} powder clearly demonstrates a noticeable difference of color. The Li_2S_6 with the $NaBH_4$-treated CeO_{2-x} powder demonstrates colorless solution in comparison with the bright yellow Li_2S_6 solution containing the untreated CeO_2 powder. The obvious color change of the Li_2S_6 solution provides convincing visual evidence of a negligible amount of polysulfides still remaining in the DOL/DME and corroborates a better polysulfides adsorption capability by the oxygen-deficient CeO_{2-x} powder [50].

After 350 galvanostatic cycles at 2C, the coin cells were disassembled aiming to gather physical evidence for polysulfides diffusion through the separator [51]. The cycled polypropylene (PP) separator with the CeO_2NR@CC cathode (Fig. 8g) that is facing sulfur cathode became slightly yellow, visibly illustrating the crossover of sulfur species through porous polymer matrix and suggesting a small quantity of polysulfides diffusion across the separator, leading to parasitic reactions between Li anode and polysulfides [52]. In contrast, yellow precipitates were hardly observed on the cycled PP separator with the CeO_{2-x}NR@CC cath-

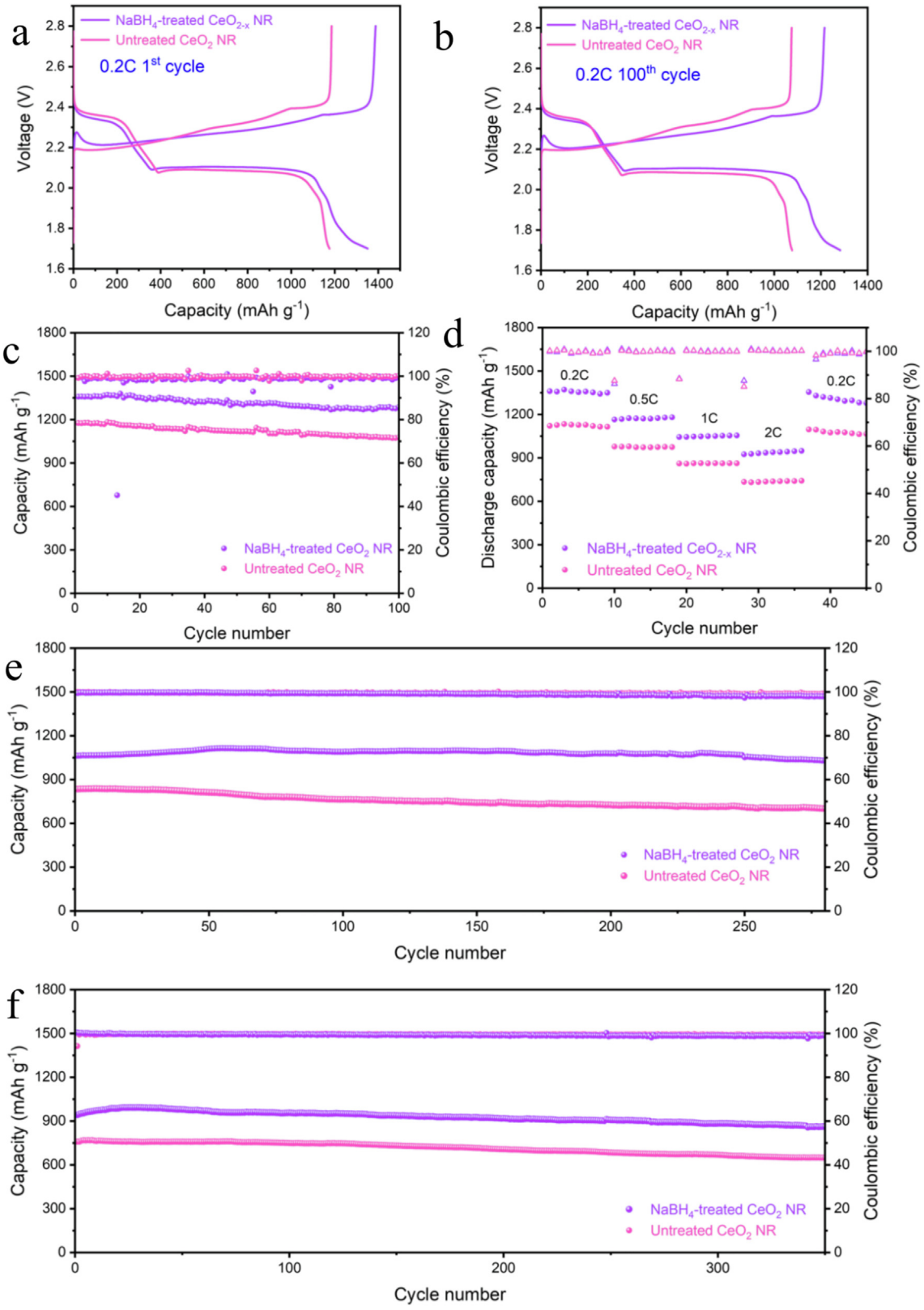

Fig. 5. Discharge profiles of the CeO_2NR@CC and CeO_{2-x}NR@CC cells at 0.2C for (a) 1st cycle and (b) 100th cycle; Cycling performances of the CeO_2NR@CC and CeO_{2-x}NR@CC cells (c) at 0.2C for 100 cycles (e) at 1C for 280 cycles (f) at 2C for 350 cycles; (d) Discharge rate capacity of the CeO_2NR@CC and CeO_{2-x}NR@CC cells at various current densities.

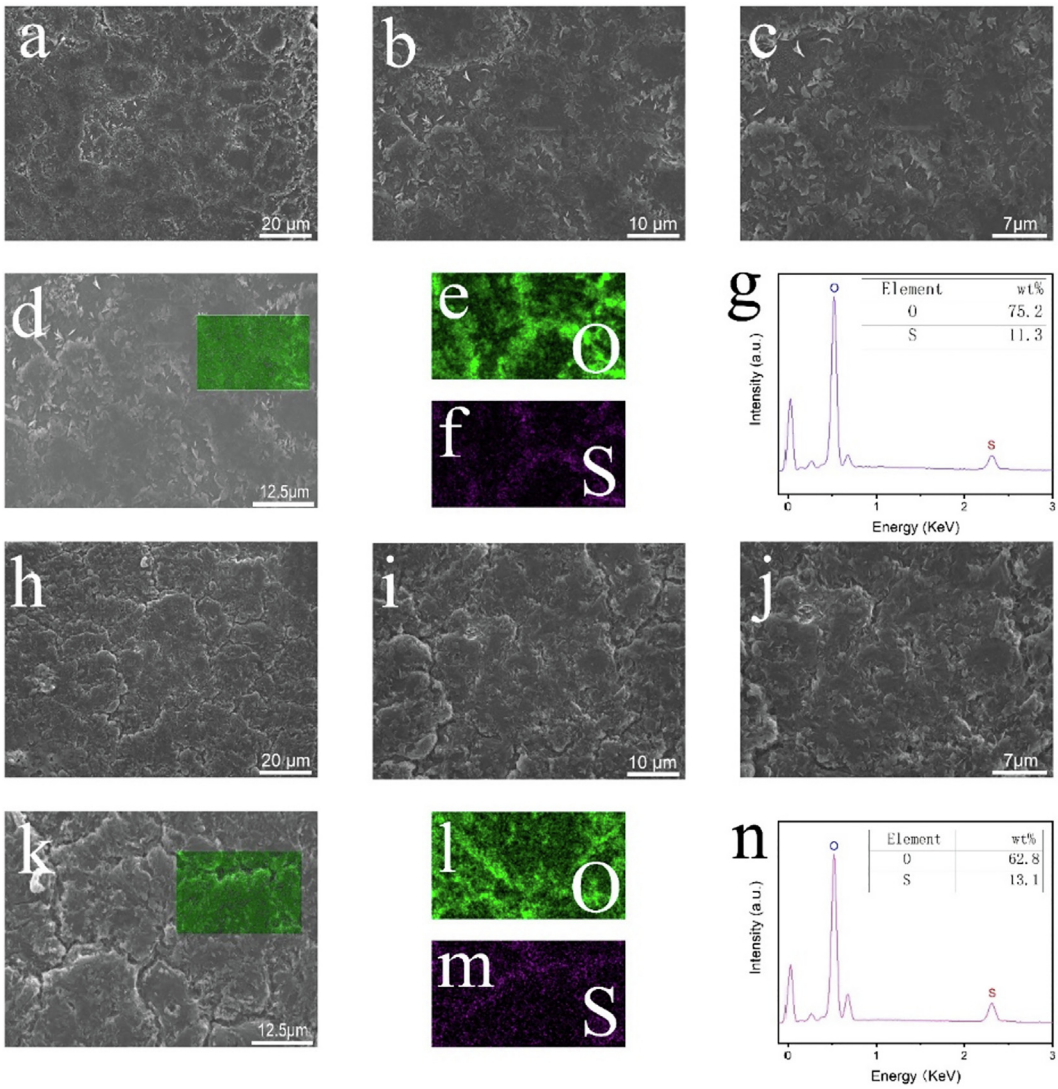

Fig. 6. (a–c) SEM images and (d–g) EDS elemental mapping of the cycled Li anode with the CeO_{2-x}NR@CC electrode; (h–j) SEM images and (k–n) EDS elemental mapping of the cycled Li anode with the CeO_2NR@CC electrode.

ode (Fig. 8f) and the cycled separator remained similar to a fresh PP separator, implying the successful prevention of polysulfide dissolution and diffusion.

3.6. Electrochemical impedance spectroscopy analysis

Electrochemical impedance spectrum (EIS) measurements before cycling and after cycling were carried out to understand the internal electrochemical redox kinetics of the CeO_{2-x}NR@CC and CeO_2NR@CC cells. Before cycling (Fig. 9a), the Nyquist plots of the CeO_{2-x}NR@CC and CeO_2NR@CC cells are composed of a semicircle in the high to medium frequency region associated with the charge transfer resistance (R_{ct}) and a straight line in the low-frequency region corresponding to the diffusion controlled Warburg impedance (W_0) [53]. The corresponding equivalent circuit model is shown in Fig. 9c. R_s is the resistance of the electrolyte, while R_{ct} and CPE_1 represent the charge transfer resistance and capacitance of the electrode/electrolyte interface, respectively. Moreover, W_0 represents the Warburg impedance, which is associated with the ion diffusion. After 350 galvanostatic cycles at 2C (Fig. 9b), the Nyquist plots of both cells demonstrate an extra semicircle. The corresponding equivalent circuit model is exhibited in Fig. 9d. R_s corresponds to the resistance of the electrolyte and W_0 corresponds to the Warburg impedance. The semicircle in the high-frequency is attributed to the interfacial (SEI:solid electrolyte interphase) resistance [54–55], which is modelled with R_1 and CPE_1, respectively. Moreover, the semicircle in the middle frequency region refers to the charge transfer process, which is modelled with R_2 and CPE_2, respectively [56–57]. Before cycling (Fig. 9a), the charge transfer resistance (R_{ct}) value of the CeO_{2-x}NR@CC cell (6.13 Ω) is much smaller than that of the CeO_2NR@CC cell (18.57 Ω), implying an accelerated charge transfer and a promoted redox reaction. After 350 galvanostatic cycles at 2C (Fig. 9b), the high-frequency semicircles of both cells clearly are smaller than those of the fresh cells, implying accelerated charge transport, successful rearrangement of the active material, and more complete electrolyte infiltration after the initial galvanostatic cycles [58]. The coin cell with CeO_{2-x}NR@CC still demonstrated a smaller charge-transfer resistance (3.80 Ω) compared with the CeO_2NR@CC cell (4.39 Ω), suggesting a smooth and faster Li^+ transfer leading to the enhanced rate performance and cycling stability of Li-S battery.

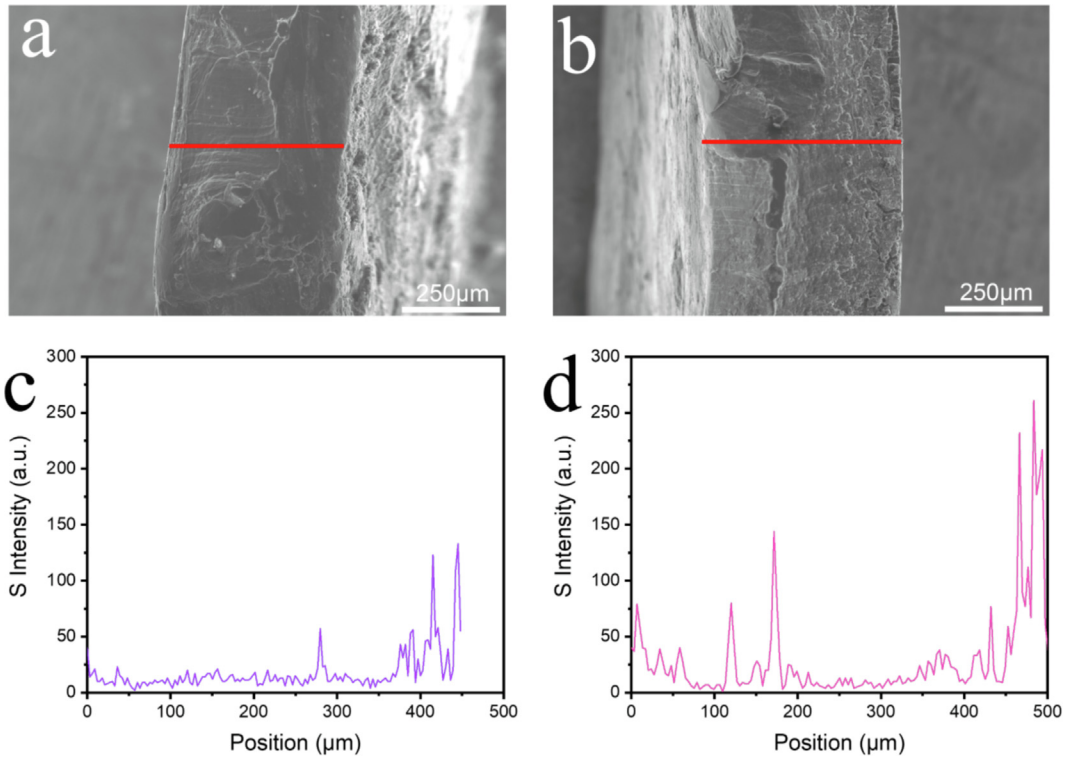

Fig. 7. The cross-section topography and cross-sectional EDS line scans (for sulfur) of the Li anodes after cycling (a and c) with the CeO_{2-x}NR@CC electrode and (b and d) with the CeO_2NR@CC electrode.

3.7. XPS analysis

XPS measurements were implemented to further understand the surface electronic structures of the $NaBH_4$-treated CeO_{2-x}NR powder and untreated CeO_2NR powder after Li_2S_6 adsorption test. The Ce 3d XPS spectra of both samples exhibit eight different deconvoluted peaks located at around 917.0, 908.0, 903.4, 901.2, 898.6, 889.0, 885.4 and 882.8 eV which correspond to v_4, v_3, v_2, v_1, u_4, u_3, u_2 and u_1 respectively (Fig. 10a–b). The u and v representative peaks signify the $3d_{5/2}$ and $3d_{3/2}$ levels, respectively [29]. The representative peaks of v_4, v_3, v_1, and u_4, u_3, u_1 are correlated with Ce^{4+} whereas the typical peaks of v_2 and u_2 are associated with the primary photoemission of Ce^{3+} [59]. It is worth mentioning that the peak area of Ce^{3+} peaks over the total area of all deconvoluted peaks ($Ce^{3+}/(Ce^{4+} + Ce^{3+})$) determines the relative amount of oxygen deficiencies on the surface of the prepared samples [60]. According to the calculation, the $NaBH_4$-treated CeO_{2-x}NR (21.8%) possesses much more oxygen vacancies than the untreated CeO_2-NR (13.9%), which confirms a significant increase in oxygen vacancies induced by a facile $NaBH_4$ solution treatment. The O 1 s spectra (Fig. 10c–d) of both samples were deconvoluted into two constituents. The O_L and O_V peaks are correlated with the oxygen in the lattice skeleton and surface oxygen vacancies, respectively [61]. The relative amount of oxygen deficiencies can be determined from the ratio of the O_V peak area to the total area of two deconvoluted peaks ($O_V/(O_V + O_L)$) [62]. Based on our calculation, the amount of the existing oxygen vacancies of the $NaBH_4$-treated CeO_{2-x}NR (70.8%) is higher than that of untreated CeO_2NR (60.7%), implying that $NaBH_4$-treated CeO_{2-x}NR possesses more oxygen vacancies than the untreated CeO_2NR.

The chemical adsorption capability of the $NaBH_4$-treated CeO_{2-x}NR powder and untreated CeO_2NR powder towards Li_2S_6 was further validated by the analysis of S 2p XPS spectra (Fig. 10e-f). Fig. 10e-f exhibit the bonds of polythionate ($[SO_3S_2SO_3]^{-2}$, ~ 170.1 eV), thiosulfate ($[S_2O_3]^{-2}$, ~ 167.8 eV), the bridging sulfur atom ($S^0{}_B$, ~ 162.6 eV) and the terminal Li-S bond ($S^{-1}{}_T$, ~ 169 eV), respectively [43,63,64]. By calculating the area proportion of complex sulfur species (polythionate and thiosulfate) in the area of all sulfur species, the sulfur adsorption capability and catalytic conversion capability can be determined [65]. Based on our calculation, the relative amount of polythionate and thiosulfate of the $NaBH_4$-treated CeO_{2-x}NR powder (63.8%) is much higher than that of the untreated CeO_2NR powder (39.6%). It is accepted now that thiosulfates $[S_2O_3]^{-2}$ and polythionates $[SO_3S_2SO_3]^{-2}$ are able to work as efficient meditators for accelerating the electrochemical conversion from polysulfides to Li_2S_2/Li_2S [66,67]. Therefore, the formation of more thiosulfates $[S_2O_3]^{-2}$ and polythionates $[SO_3S_2SO_3]^{-2}$ further confirms that $NaBH_4$-treated CeO_{2-x}NR powder has better capability to curtail sulfur mass loss.

3.8. Proposed working mechanism

As shown in Fig. 11, we propose an underlying working mechanism of polysulfides adsorbed on CeO_2 NR and defect-rich CeO_{2-x}NR. CeO_2 NR and defect-rich CeO_{2-x}NR are denoted by yellow and purple, respectively. Inside of the black box, oxygen vacancies can be found and are firmly anchored on the terminal planes. Outside of the black box, oxygen deficiencies cannot be seen, and the normal terminal planes are shown. The number of black boxes of defect-rich CeO_{2-x}NR is larger than that of CeO_2 NR, suggesting that defect-rich CeO_{2-x}NR possesses more oxygen vacancies than CeO_2 NR does. According to our previously published work [25], the Ce-S and Li-O chemical bonding was successfully constructed on the (1 1 0) terminal facet of CeO_2 NR during charge–discharge process, leading to the efficient restriction of polysulfides migration.

It is well known that the electronic structures along with the ion energetics and electronic transfer in CeO_2 can be notably

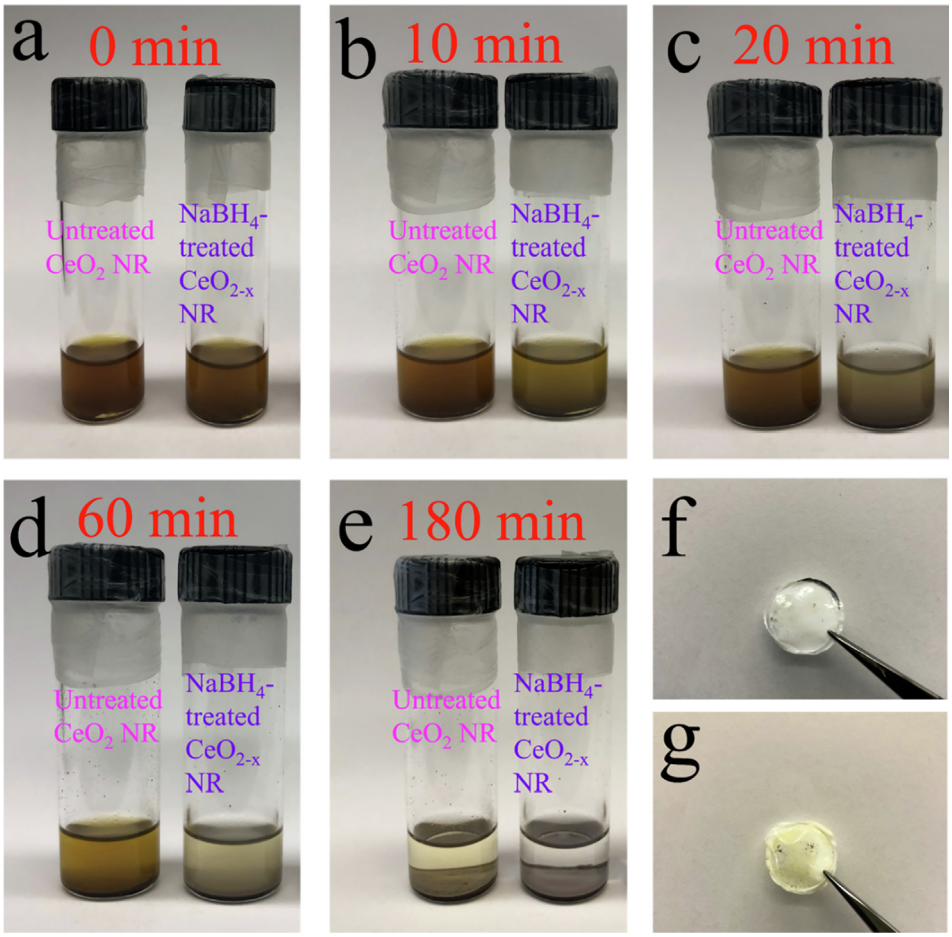

Fig. 8. Optical images of Li_2S_6 solution adsorption tests containing (a) untreated CeO_2 NR powder and $NaBH_4$-treated CeO_{2-x} NR powder: (a) at the time = 0 min; (b) at the time = 10 min; (c) at the time = 20 min; (d) at the time = 60 min; (e) at the time = 180 min. The digital images of the cycled separators: (f) with the CeO_{2-x}NR@CC electrode and (g) with the CeO_2NR@CC electrode.

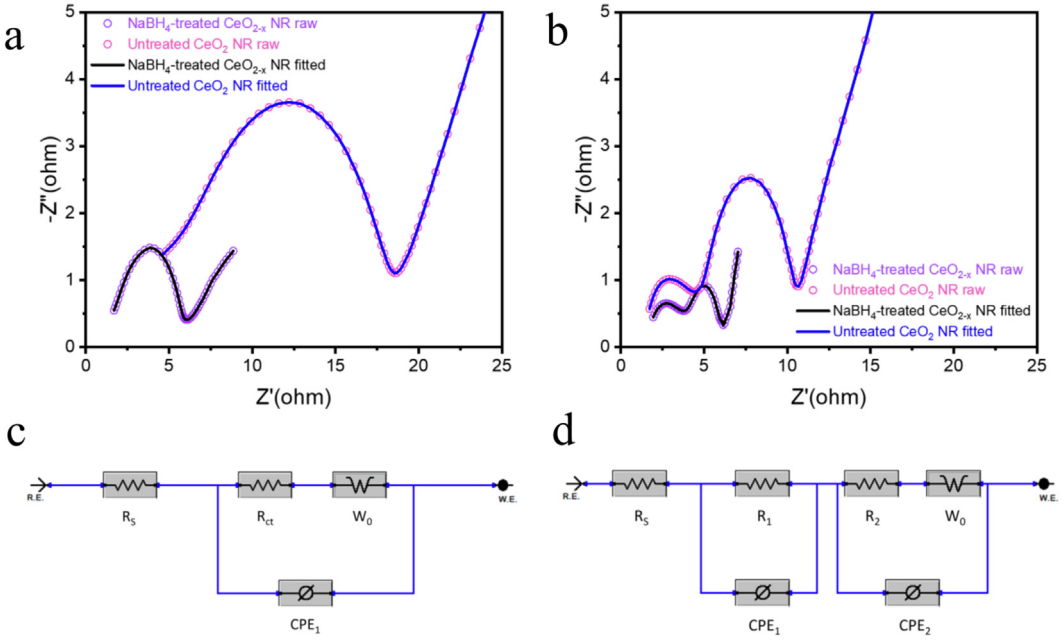

Fig. 9. EIS curves of the cells with $NaBH_4$-treated CeO_{2-x}NR and untreated CeO_2NR: (a) before cycling (b) after cycling. Equivalent circuit model: (c) before cycling and (d) after cycling.

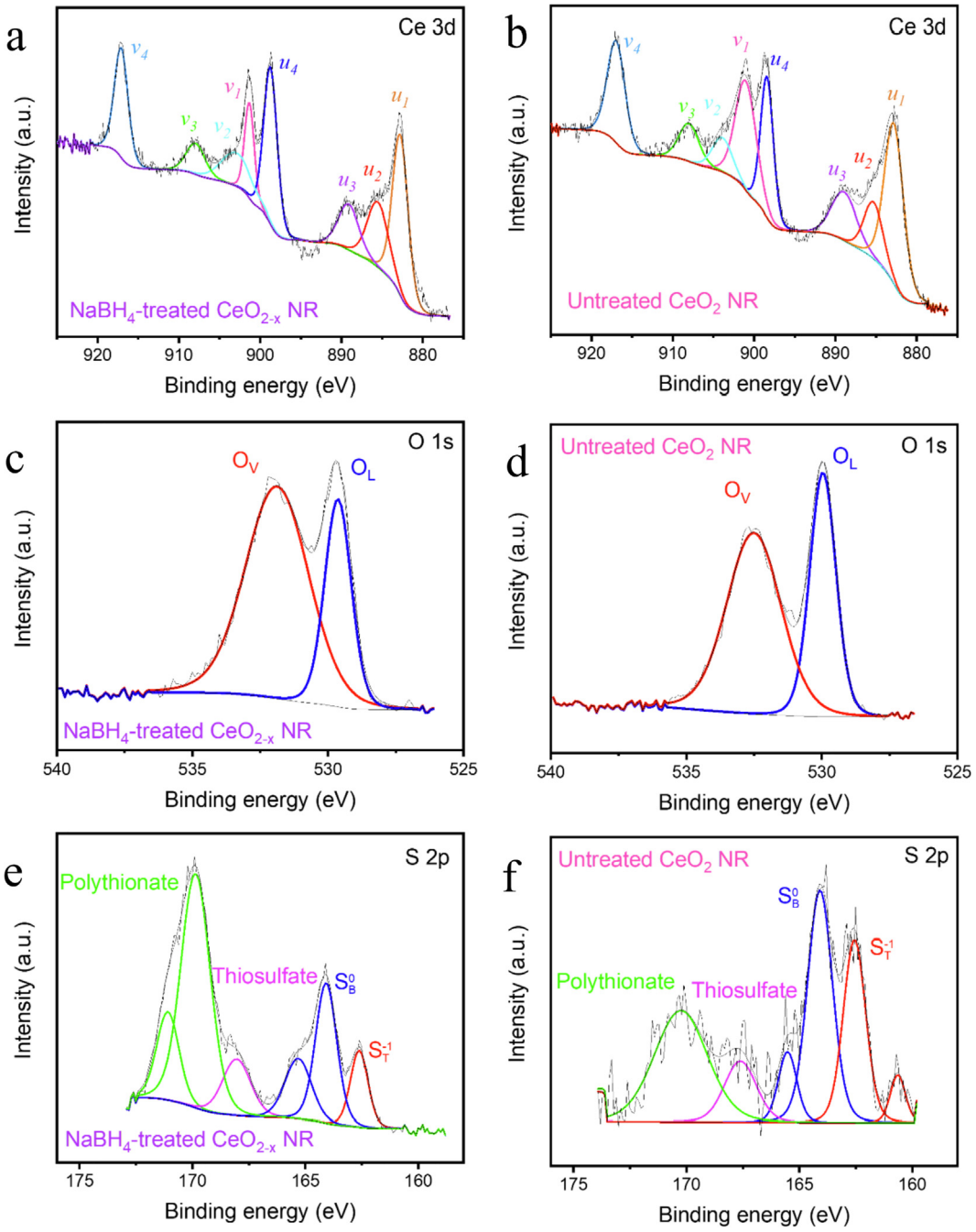

Fig. 10. XPS spectra of (a–b) Ce 3d, (c–d) O 1 s, and (e–f) S 2p of the $NaBH_4$-treated CeO_{2-x}NR powder and untreated CeO_2NR powder after Li_2S_6 adsorption test.

altered by the presence of oxygen vacancies and Ce^{3+}/Ce^{4+} pairs. Furthermore, the band gap of CeO_2 can be significantly shrunk by oxygen vacancies. Therefore, the facilitated charge transfer from framework to adsorbates can be fulfilled by the decrease in the energy barrier of interfacial charge transfer. Accordingly, the better chemical interaction against polysulfides and catalytic conversion capability can be fulfilled by implanting abundant oxygen vacancies that not only can notably improve the electronic conductivity of CeO_2 NR but also can provide numerous unsaturated bonds at the surface of CeO_2 NR. Therefore, even though CeO_2 NR possesses the terminal plane (110), (100) and defected (111) with strong adsorption capability towards polysulfides, limited restriction of polysulfides migration and unsatisfactory catalytic conversion are observed especially at high-current density due to insufficient oxygen deficiencies that can fulfill the alteration of electronic structure and the enhancement of catalytic transformation.

We believe that the main reason for the trigged formation of thiosulfate and polythionate species is due to the oxygen vacancies and/or other surface defects on CeO_2 nanorods, which can strengthen the chemical bond with polysulfides (i.e., Li-O bond). For instance, Zhang et al. [68] reported that oxygen-deficient Ta_2O_{5-x} shows significantly improved electrochemical performance compared with pristine Ta_2O_5, which was confirmed by DFT simulation. Their DFT data exhibits that the pristine Ta_2O_5 (001) demonstrates a relatively low Li_2S_6 adsorption energy (E_{ads}) of −0.83 eV with a Li–O bond length of 2.52 Å, leading to limited

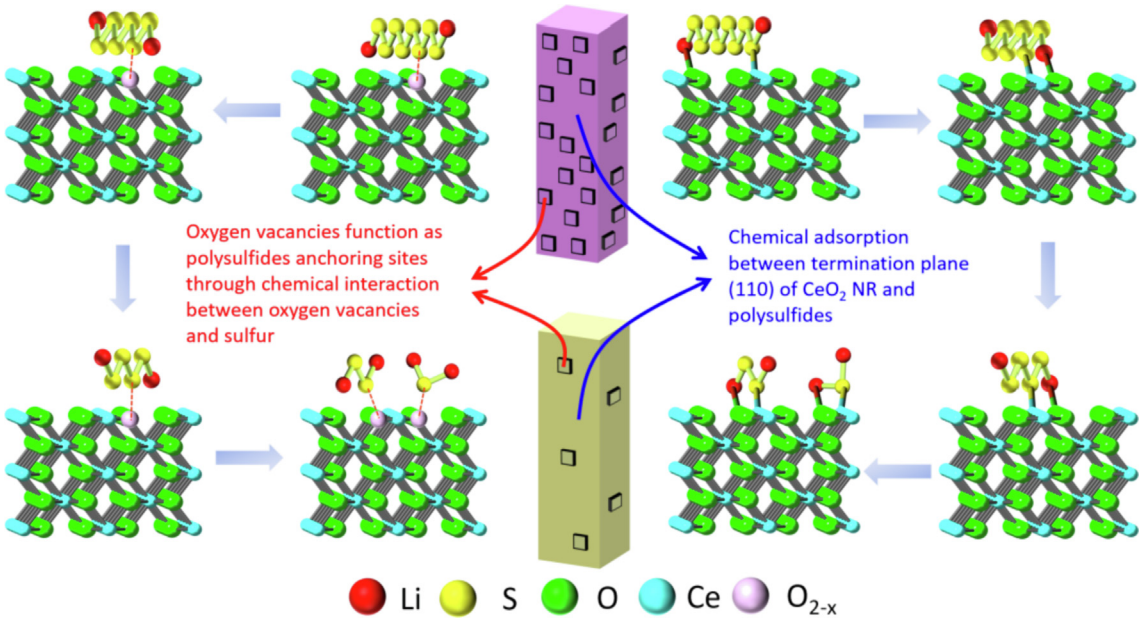

Fig. 11. Schematic illustration of possible working mechanism of pristine CeO_2 NR and oxygen-deficient CeO_{2-x}NR against lithium polysulfides.

restriction of polysulfides. However, the defective structure significantly enhances the Li_2S_6 binding energy with a higher E_{ads} (−2.0 eV) and notably strengthened Li–O bond (1.86 Å), suggesting the superb polysulfides restriction on of Ta_2O_{5-x} with oxygen vacancies. In addition, Luo et al. [69] reported that oxygen-deficient Nb_2O_{5-x} demonstrates notably improved chemical bonding with polysulfides compared to pristine Nb_2O_5, which was also substantiated by DFT simulation. The same cleave surface was selected in pristine Nb_2O_5 and oxygen-deficient Nb_2O_{5-x} to compare its surface adsorption capability towards polysulfides. Clearly, pristine Nb_2O_5 displays a moderate E_{ads} of −1.75 eV with a Li—O bond distance of 2.38 Å. In contrast, the DFT calculation of Nb_2O_{5-x} (001) exhibits a much higher E_{ads} of −3.38 eV with a reduced Li—O bond length (1.87 Å), suggesting the improved polysulfides affinity on oxygen vacancies. Once polysulfides are chemically anchored on the surface, thiosulfates are produced by the oxidation of polysulfides on the host. Subsequently, newly formed long-chain polysulfides are immobilized by thiosulfate to form polythionates and reduced into insoluble short-chain polysulfides [4].

4. Conclusion

In summary, compared with other complicated and costly methods, we have successfully introduced copious oxygen vacancies onto the surface of CeO_2 NR through a facile $NaBH_4$ solution treatment method. For CeO_2NR@CC, with the combination of (110), (100) and defected (111) terminal planes, the limited number of oxygen vacancies cannot guarantee favorable electrochemical properties after long cycling. In contrast to the CeO_2NR@CC control sample, the CeO_{2-x}NR@CC electrode with much more embedded oxygen deficiencies not only dramatically narrows the band gap and tunes the electronic structure, but also efficiently utilizes copious oxygen vacancies to adsorb more polysulfides. The distinguishable electrochemical performance difference between the CeO_2NR@CC control and the CeO_{2-x}NR@CC electrode can be easily observed. For example, the CeO_2 NR@CC exhibits an initial capacity of 759 mAh g^{-1} and reversible capacity of 650 mAh g^{-1} after 350 cycles at 2C, suggesting a moderate capacity retention of 85.6%. In contrast, for the CeO_{2-x} NR@CC electrode, an exceptional initial capacity of 943 mAh g^{-1} and extraordinary reversible capacity of 863 mAh g^{-1} after 350 cycles are displayed. The resulting capacity retention is as high as 91.5% and the corresponding capacity degradation rate is merely 0.024% per cycle in a long-term 350 cycles. Therefore, it can be concluded that the introduction of copious oxygen vacancies through a facile and cost-effective $NaBH_4$ solution treatment imposes a significantly positive impact on the improvement of electrochemical properties, providing a novel concept for the rational tunability of metal oxides for high-energy and high-power Li-S batteries.

CRediT authorship contribution statement

Zhen Wei: Investigation, Methodology, Formal analysis, Writing – original draft, Writing – review & editing. **Ruigang Wang:** Conceptualization, Investigation, Methodology, Supervision, Formal analysis, Writing – review & editing, Funding acquisition.

Declaration of Competing Interest

The authors declare that they have no known competing financial interests or personal relationships that could have appeared to influence the work reported in this paper.

Acknowledgment

This work is supported by the National Science Foundation (CBET-2118784 and IIP-2147564). This project also receives partial financial support from Alabama Transportation Institute and Alabama Water Institute. The use of electron microscopy facilities at the Alabama Analytical Research Center (AARC), The University of Alabama, is gratefully acknowledged.

Appendix A. Supplementary material

Supplementary data to this article can be found online at https://doi.org/10.1016/j.jcis.2022.01.165.

References:

[1] J. He, A. Manthiram, A review on the status and challenges of electrocatalysts in lithium-sulfur batteries, Energy Storage Mater. 20 (2019) 55–70.

[2] L. Yang, H. Li, Q. Li, Y. Wang, Y. Chen, Z. Wu, Y. Liu, G. Wang, B. Zhong, W. Xiang, Y. Zhong, X. Guo, Research Progress on Improving the Sulfur Conversion Efficiency on the Sulfur Cathode Side in Lithium-Sulfur Batteries, Ind. Eng. Chem. Res. 59 (2020) 20979–21000.

[3] L. Zhang, Y. Wang, Z. Niu, J. Chen, Advanced nanostructured carbon-based materials for rechargeable lithium-sulfur batteries, Carbon 141 (2019) 400–416.

[4] M. Zhang, W. Chen, L. Xue, Y. Jiao, T. Lei, J. Chu, J. Huang, C. Gong, C. Yan, Y. Yan, Y. Hu, X. Wang, J. Xiong, Adsorption-Catalysis Design in the Lithium-Sulfur Battery, Adv. Energy Mater. 10 (2019) 1903008.

[5] L. Chen, L.L. Shaw, Recent advances in lithium–sulfur batteries, J. Power Sources 267 (2014) 770–783.

[6] A. Manthiram, S.-H. Chung, C. Zu, Lithium-sulfur batteries: progress and prospects, Adv Mater 27 (12) (2015) 1980–2006.

[7] J. Choi, T.-G. Jeong, D. Lee, S.H. Oh, Y. Jung, Y.-T. Kim, Enhanced rate capability due to highly active Ta2O5 catalysts for lithium sulfur batteries, J. Power Sources 435 (2019) 226707.

[8] G. Feng, X. Liu, Z. Wu, Y. Chen, Z. Yang, C. Wu, X. Guo, B. Zhong, W. Xiang, J. Li, Enhancing performance of Li–S batteries by coating separator with MnO @ yeast-derived carbon spheres, J. Alloy. Compd. 817 (2020) 152723.

[9] R. Yang, H. Du, Z. Lin, L. Yang, H. Zhu, H. Zhang, Z. Tang, X. Gui, ZnO nanoparticles filled tetrapod-shaped carbon shell for lithium-sulfur batteries, Carbon 141 (2019) 258–265.

[10] L. Fan, H. Wu, X. Wu, M. Wang, J. Cheng, N. Zhang, Y. Feng, K. Sun, Fe-MOF derived jujube pit like Fe3O4/C composite as sulfur host for lithium-sulfur battery, Electrochimica Acta 295 (2019) 444–451.

[11] M. Zhu, S. Li, J. Liu, B. Li, Promoting polysulfide conversion by V2O3 hollow sphere for enhanced lithium-sulfur battery, Appl. Surf. Sci. 473 (2019) 1002–1008.

[12] W. Dong, D.i. Wang, X. Li, Y. Yao, X.u. Zhao, Z. Wang, H.-E. Wang, Y.u. Li, L. Chen, D. Qian, B.-L. Su, Bronze TiO2 as a cathode host for lithium-sulfur batteries, J. Energy Chem. 48 (2020) 259–266.

[13] H. Chen, W.-D. Dong, F.-J. Xia, Y.-J. Zhang, M. Yan, J.-P. Song, W. Zou, Y. Liu, Z.-Y. Hu, J. Liu, Y.u. Li, H.-E. Wang, L.-H. Chen, B.-L. Su, Hollow nitrogen-doped carbon/sulfur@ MnO2 nanocomposite with structural and chemical dual-encapsulation for lithium-sulfur battery, Chem. Eng. J. 381 (2020) 122746, https://doi.org/10.1016/j.cej.2019.122746.

[14] H.-E. Wang, K. Yin, N. Qin, X.u. Zhao, F.-J. Xia, Z.-Y. Hu, G. Guo, G. Cao, W. Zhang, Oxygen-deficient titanium dioxide as a functional host for lithium–sulfur batteries, J. Mater. Chem. A 7 (17) (2019) 10346–10353.

[15] H.-E. Wang, K. Yin, X.u. Zhao, N. Qin, Y.u. Li, Z. Deng, L. Zheng, B.-L. Su, Z. Lu, Coherent TiO 2/BaTiO 3 heterostructure as a functional reservoir and promoter for polysulfide intermediates, Chem. Commun. 54 (86) (2018) 12250–12253.

[16] L. Meng, Y. Yao, J. Liu, Z. Wang, D. Qian, L. Zheng, B.-L. Su, H.-E. Wang, MoSe2 nanosheets as a functional host for lithium-sulfur batteries, J. Energy Chem. 47 (2020) 241–247.

[17] H.-E. Wang, X. Li, N. Qin, X.u. Zhao, H. Cheng, G. Cao, W. Zhang, Sulfur-deficient MoS2 grown inside hollow mesoporous carbon as a functional polysulfide mediator, J. Mater. Chem. A 7 (19) (2019) 12068–12074.

[18] Y. Tian, G. Li, Y. Zhang, D. Luo, X. Wang, Y. Zhao, H. Liu, P. Ji, X. Du, J. Li, Z. Chen, Low-Bandgap Se-Deficient Antimony Selenide as a Multifunctional Polysulfide Barrier toward High-Performance Lithium-Sulfur Batteries, Adv. Mater. 32 (4) (2020) 1904876, https://doi.org/10.1002/adma.v32.410.1002/adma.201904876.

[19] J. Wang, G. Li, D. Luo, Y. Zhang, Y. Zhao, G. Zhou, L. Shui, X. Wang, Z. Chen, Engineering the Conductive Network of Metal Oxide-Based Sulfur Cathode toward Efficient and Longevous Lithium-Sulfur Batteries, Adv. Energy Mater. 10 (41) (2020) 2002076, https://doi.org/10.1002/aenm.v10.4110.1002/aenm.202002076.

[20] J. Zhao, D. Zhao, L. Li, L.i. Zhou, X. Liang, Z. Wu, Z.-J. Jiang, Defect-rich, mesoporous cobalt sulfide hexagonal nanosheets as superior sulfur hosts for high-rate, long-cycle rechargeable lithium–sulfur batteries, J. Phys. Chem. C 124 (23) (2020) 12259–12268.

[21] T. Yang, K. Liu, T. Wu, J. Zhang, X. Zheng, C. Wang, M. Chen, Rational valence modulation of bimetallic carbide assisted by defect engineering to enhance polysulfide conversion for lithium–sulfur batteries, J. Mater. Chem. A 8 (35) (2020) 18032–18042.

[22] K. Lv, P. Wang, C. Wang, Z. Shen, Z. Lu, H. Zhang, M. Zheng, P. He, H. Zhou, Oxygen-Deficient Ferric Oxide as an Electrochemical Cathode Catalyst for High-Energy Lithium-Sulfur Batteries, Small 16 (22) (2020) 2000870, https://doi.org/10.1002/smll.v16.2210.1002/smll.202000870.

[23] Y. Li, X. Zhang, G. Liu, A. Gerhardt, K. Evans, A. Jia, Z. Zhang, Oxygen-deficient titanium dioxide supported cobalt nano-dots as efficient cathode material for lithium-sulfur batteries, Journal of Energy, Chemistry 48 (2020) 390–397.

[24] J. Wang, W. Wang, Y. Zhang, Z. Bakenov, Y. Zhao, X. Wang, Synthesis of highly defective hollow double-shelled Co3O4−x microspheres as sulfur host for high-performance lithium-sulfur batteries, Mater. Lett. 255 (2019) 126581, https://doi.org/10.1016/j.matlet.2019.126581.

[25] Z. Wei, J. Li, Y. Wang, R. Wang, High-performance Li-S batteries enabled by polysulfide-infiltrated free-standing 3D carbon cloth with CeO2 nanorods decoration, Electrochimica Acta 388 (2021) 138645, https://doi.org/10.1016/j.electacta.2021.138645.

[26] R. Wang, R. Dangerfield, Seed-mediated synthesis of shape-controlled CeO2nanocrystals, RSC Adv. 4 (7) (2014) 3615–3620.

[27] J. Li, Z. Liu, R. Wang, Support structure and reduction treatment effects on CO oxidation of SiO2 nanospheres and CeO2 nanorods supported ruthenium catalysts, J Colloid Interface Sci 531 (2018) 204–215.

[28] S.T. Hossain, E. Azeeva, K. Zhang, E.T. Zell, D.T. Bernard, S. Balaz, R. Wang, A comparative study of CO oxidation over Cu-O-Ce solid solutions and CuO/CeO2 nanorods catalysts, Appl. Surf. Sci. 455 (2018) 132–143.

[29] S.T. Hossain, Y. Almesned, K. Zhang, E.T. Zell, D.T. Bernard, S. Balaz, R. Wang, Support structure effect on CO oxidation: A comparative study on SiO2 nanospheres and CeO2 nanorods supported CuOx catalysts, Appl. Surf. Sci. 428 (2018) 598–608.

[30] R. Gao, Z. Shang, L. Zheng, J. Wang, L. Sun, Z. Hu, X. Liu, Enhancing the Catalytic Activity of Co3O4 Nanosheets for Li-O2 Batteries by the Incoporation of Oxygen Vacancy with Hydrazine Hydrate Reduction, Inorg Chem 58 (8) (2019) 4989–4996.

[31] S. Zhang, G. Wang, J. Jin, L. Zhang, Z. Wen, J. Yang, Self-catalyzed decomposition of discharge products on the oxygen vacancy sites of MoO3 nanosheets for low-overpotential Li-O2 batteries, NANO Energy 36 (2017) 186–196.

[32] Z. Sadighi, J. Huang, L. Qin, S. Yao, J. Cui, J.-K. Kim, Positive role of oxygen vacancy in electrochemical performance of CoMn 2 O 4 cathodes for Li-O 2 batteries, J. Power Sources 365 (2017) 134–147.

[33] Z. Liu, J. Li, R. Wang, CeO2 nanorods supported M-Co bimetallic oxides (M = Fe, Ni, Cu) for catalytic CO and C3H8 oxidation, J. Colloid Interface Sci. 560 (2020) 91–102.

[34] Y. Tian, X. Zhang, Y. Zhang, J. Li, A. Jia, G. Liu, Z. Bakenov, Cobalt-doped oxygen-deficient titanium dioxide coated by carbon layer as high-performance sulfur host for Li/S batteries, J. Alloy. Compd. 861 (2021) 157969.

[35] Z. Li, R. Xu, S. Deng, X. Su, W. Wu, S. Liu, M. Wu, MnS decorated N/S codoped 3D graphene which used as cathode of the lithium-sulfur battery, Appl. Surf. Sci. 433 (2018) 10–15.

[36] Y. Wu, W. Zhang, T. Han, Z. Shen, D. Cheng, H. Zhang, J. Li, H. Zhang, J. Liu, A novel ternary sulfur/carbon@tin dioxide composite with polysulfides-adsorptive shell and conductive core as high-performance lithium-sulfur battery cathodes, Appl. Surf. Sci. 489 (2019) 462–469.

[37] Y.u. You, M. Wei, L. Yang, J. Wang, Y. Zhang, J. Xu, Multifunctional MoSe2@rGO coating on the cathode versus the separator as an efficient polysulfide barrier for high-performance lithium-sulfur battery, Appl. Surf. Sci. 527 (2020) 146785, https://doi.org/10.1016/j.apsusc.2020.146785.

[38] L. Chen, C. Xu, L. Yang, M. Zhou, B. He, Z. Chen, Z. Li, M. Shi, Z. Hou, Y. Kuang, Nitrogen-doped holey carbon nanotubes: Dual polysulfides trapping effect towards enhanced lithium-sulfur battery performance, Appl. Surf. Sci. 454 (2018) 284–292.

[39] X. Wu, L. Fan, M. Wang, J. Cheng, H. Wu, B. Guan, N. Zhang, K. Sun, Long-Life Lithium-Sulfur Battery Derived from Nori-Based Nitrogen and Oxygen Dual-Doped 3D Hierarchical Biochar, ACS Appl Mater Interfaces 9 (22) (2017) 18889–18896.

[40] J. Li, Z. Niu, Y. Chen, Q. Zhou, Y. Yan, C. Guo, M. Li, Mn3(PO4)2/rGO as dual-function polysulfide inhibitor through oxygen deficiencies and polar sites for lithium sulfur batteries, Appl. Surf. Sci. 521 (2020) 146425, https://doi.org/10.1016/j.apsusc.2020.146425.

[41] W. Yao, C. Chu, W. Zheng, L. Zhan, Y. Wang, "Pea-pod-like" nitrogen-doped hollow porous carbon cathode hosts decorated with polar titanium dioxide nanocrystals as efficient polysulfide reservoirs for advanced lithium–sulfur batteries, J. Mater. Chem. A 6 (37) (2018) 18191–18205.

[42] H. Lin, S. Zhang, T. Zhang, H. Ye, Q. Yao, G.W. Zheng, J.Y. Lee, Elucidating the Catalytic Activity of Oxygen Deficiency in the Polysulfide Conversion Reactions of Lithium-Sulfur Batteries, Adv. Energy Mater. 8 (30) (2018) 1801868, https://doi.org/10.1002/aenm.v8.3010.1002/aenm.201801868.

[43] W. Yao, W. Zheng, J. Xu, C. Tian, K. Han, W. Sun, S. Xiao, ZnS-SnS@NC Heterostructure as Robust Lithiophilicity and Sulfiphilicity Mediator toward High-Rate and Long-Life Lithium-Sulfur Batteries, ACS Nano 15 (4) (2021) 7114–7130.

[44] M. Li, X. Li, V. Tung, Y. Li, Z. Lai, Protection of Lithium Anode by a Highly Porous PVDF Membrane for High-Performance Li–S Battery, ACS Applied Energy Materials 3 (3) (2020) 2510–2515.

[45] G. Ma, Z. Wen, J. Jin, M. Wu, X. Wu, J. Zhang, Enhanced cycle performance of Li–S battery with a polypyrrole functional interlayer, J. Power Sources 267 (2014) 542–546.

[46] Y. Lu, S. Gu, X. Hong, K. Rui, X. Huang, J. Jin, C. Chen, J. Yang, Z. Wen, Pre-modified Li3PS4 based interphase for lithium anode towards high-performance Li-S battery, Energy Storage Mater. 11 (2018) 16–23.

[47] J. Li, L. Zhang, F. Qin, B.o. Hong, Q. Xiang, K. Zhang, J. Fang, Y. Lai, ZrO (NO3) 2 as a functional additive to suppress the diffusion of polysulfides in lithium-sulfur batteries, J. Power Sources 442 (2019) 227232, https://doi.org/10.1016/j.jpowsour.2019.227232.

[48] C. Du, J. Wu, P.u. Yang, S. Li, J. Xu, K. Song, Embedding S@TiO2 nanospheres into MXene layers as high rate cyclability cathodes for lithium-sulfur batteries, Electrochimica Acta 295 (2019) 1067–1074.

[49] P. Shi, Y. Wang, X. Liang, Y.i. Sun, S. Cheng, C. Chen, H. Xiang, Simultaneously Exfoliated Boron-Doped Graphene Sheets To Encapsulate Sulfur for Applications in Lithium-Sulfur Batteries, ACS Sustainable Chem. Eng. 6 (8) (2018) 9661–9670.

[50] T. Lei, W. Chen, J. Huang, C. Yan, H. Sun, C. Wang, W. Zhang, Y. Li, J. Xiong, Multi-Functional Layered WS2Nanosheets for Enhancing the Performance of Lithium-Sulfur Batteries, Adv. Energy Mater. 7 (4) (2017) 1601843, https://doi.org/10.1002/aenm.201601843.
[51] H. Shao, W. Wang, H. Zhang, A. Wang, X. Chen, Y. Huang, Nano-TiO2 decorated carbon coating on the separator to physically and chemically suppress the shuttle effect for lithium-sulfur battery, J. Power Sources 378 (2018) 537–545.
[52] P.-Y. Zhai, H.-J. Peng, X.-B. Cheng, L. Zhu, J.-Q. Huang, W. Zhu, Q. Zhang, Scaled-up fabrication of porous-graphene-modified separators for high-capacity lithium–sulfur batteries, Energy Storage Mater. 7 (2017) 56–63.
[53] R. Zhuang, S. Yao, X. Shen, T. Li, Hydrothermal synthesis of mesoporous MoO2 nanospheres as sulfur matrix for lithium sulfur battery, Journal of Electroanalytical Chemistry 833 (2019) 441–448.
[54] Z. Ye, Y. Jiang, T. Feng, Z. Wang, L.i. Li, F. Wu, R. Chen, Curbing polysulfide shuttling by synergistic engineering layer composed of supported Sn4P3 nanodots electrocatalyst in lithium-sulfur batteries, NANO Energy 70 (2020) 104532, https://doi.org/10.1016/j.nanoen.2020.104532.
[55] Z. Deng, Z. Zhang, Y. Lai, J. Liu, J. Li, Y. Liu, Electrochemical impedance spectroscopy study of a lithium/sulfur battery: modeling and analysis of capacity fading, J. Electrochem. Soc. 160 (4) (2013) A553–A558.
[56] N.A. Canas, K. Hirose, B. Pascucci, N. Wagner, K.A. Friedrich, R. Hiesgen, Investigations of lithium–sulfur batteries using electrochemical impedance spectroscopy, Electrochimica Acta 97 (2013) 42–51.
[57] Q. Peng, F. Yu, W. Wang, A. Wang, F. Wang, Y. Huang, Ultralight polyethylenimine/porous carbon modified separator as an effective polysulfide-blocking barrier for lithium-sulfur battery, Electrochimica Acta 299 (2019) 749–755.
[58] J. Tu, H. Li, T. Lan, S.-Z. Zeng, J. Zou, Q. Zhang, X. Zeng, Facile synthesis of TiN nanocrystals/graphene hybrid to chemically suppress the shuttle effect for lithium-sulfur batteries, J. Alloy. Compd. 822 (2020) 153751.
[59] S.T. Hossain, E.T. Zell, S. Balaz, R. Wang, A γ to α type transition of CuO species over CeO2-SiO2 composites supported CuO catalysts, Appl. Surf. Sci. 491 (2019) 374–382.
[60] Y. Wang, Z. Liu, M.P. Confer, J. Li, R. Wang, In-situ DRIFTS study of chemically etched CeO2 nanorods supported transition metal oxide catalysts, Molecular Catalysis 509 (2021) 111629.
[61] R. Ranganathan, Z. Liu, H. Menon, S. Talukdar, R. Wang, M. Uddi, Nanoshaped CeO2 and SiO2 supported Ru catalyst for plasma catalysis chemical looping reactions, Int. j. energy eng. 10 (2020) 67–79.
[62] Z. Liu, Y. Lu, M.P. Confer, H. Cui, J. Li, Y. Li, Y. Wang, S.C. Street, E.K. Wujcik, R. Wang, Thermally Stable RuO x–CeO2 Nanofiber Catalysts for Low-Temperature CO Oxidation, ACS Applied Nano Materials 3 (8) (2020) 8403–8413.
[63] D.K. Lee, Y. Chae, H. Yun, C.W. Ahn, J.W. Lee, CO2-Oxidized Ti3C2Tx-MXenes Components for Lithium-Sulfur Batteries: Suppressing the Shuttle Phenomenon through Physical and Chemical Adsorption, ACS Nano 14 (8) (2020) 9744–9754.
[64] F. Ma, Y. Wan, X. Wang, X. Wang, J. Liang, Z. Miao, T. Wang, C. Ma, G. Lu, J. Han, Y. Huang, Q. Li, Bifunctional Atomically Dispersed Mo-N2/C Nanosheets Boost Lithium Sulfide Deposition/Decomposition for Stable Lithium-Sulfur Batteries, ACS Nano 14 (8) (2020) 10115–10126.
[65] J. Wu, Q. Ma, C. Lian, Y. Yuan, D. Long, Promoting polythionate intermediates formation by oxygen-deficient manganese oxide hollow nanospheres for high performance lithium-sulfur batteries, Chem. Eng. J. 370 (2019) 556–564.
[66] W. Sun, X. Ou, X. Yue, Y. Yang, Z. Wang, D. Rooney, K. Sun, A simply effective double-coating cathode with MnO 2 nanosheets/graphene as functionalized interlayer for high performance lithium-sulfur batteries, Electrochimica Acta 207 (2016) 198–206.
[67] Z. Kong, Y. Li, Y. Wang, Y. Zhang, K. Shen, X. Chu, H. Wang, J. Wang, L. Zhan, Monodispersed MnOx-CeO2 solid solution as superior electrocatalyst for Li2S precipitation and conversion, Chem. Eng. J. 392 (2020) 123697.